Exsolution of Metallic Ru Nanoparticles from Defective, Fluorite-Type Solid Solutions Sm2RuxCe2–xO7 To Impart Stability on Dry Reforming Catalysts

Journal Article

Author(s):
Naeem, Muhammad A.; Abdala, Paula M.; Armutlulu, Andac; Kim, Sung Min; Fedorov, Alexey; Müller, Christoph R.

Publication date:
2020-02-07

Permanent link:
https://doi.org/10.3929/ethz-b-000404447

Originally published in:
ACS Catalysis 10(3), https://doi.org/10.1021/acscatal.9b04555

Funding acknowledgement:
156015 - Next generation CaO-based CO2 sorbents: X-ray absorption spectroscopy and advanced electron microscopy techniques (SNF)

Exsolution of Metallic Ru Nanoparticles from Defective, Fluorite-type Solid Solutions $Sm_2Ru_xCe_{2-x}O_7$ to Impart Stability on Dry Reforming Catalysts

Muhammad A. Naeem,[†] Paula M. Abdala,*[†] Andac Armutlulu,[†] Sung Min Kim,[†] Alexey Fedorov, [†] and Christoph R. Müller*[†]

[†] Department of Mechanical and Process Engineering, ETH Zürich, CH 8092 Zürich, Switzerland

KEYWORDS: reductive exsolution, dry reforming of methane, X-ray absorption spectroscopy, Ru nanoparticles, catalysis

ABSTRACT: A key challenge in the catalytic conversion of CH_4 and CO_2 into a synthesis gas (CO and H_2) via the dry reforming of methane (DRM) is the development of stable catalysts. We demonstrate that the reductive exsolution of metallic Ru from fluorite-type solid solutions $Sm_2Ru_xCe_{2-x}O_7$ (x = 0, 0.1, 0.2, 0.4) yields catalysts with high activity and remarkable stability for the DRM. The catalysts feature Ru(0) nanoparticles of ca. 1-2 nm in diameter that are uniformly dispersed on the surface of the resulting oxide support. The exsolved material was interrogated by synchrotron X-ray diffraction (XRD), X-ray absorption spectroscopy (XAS at Ru, Sm and Ce K-edges), Raman spectroscopy and transmission electron microscopy (TEM). Operando XAS-XRD experiments revealed that the exsolution of metallic ruthenium is accompanied by a rearrangement of the oxygen vacancies within the lattice. The catalysts derived through exsolution outperform (stable over 4 days) the reference catalysts prepared by wetness impregnation and sodium borohydride reduction. The superior performance of the exsolved catalysts is explained by their high resistance to sintering-induced deactivation owing to the stabilizing metal-support interaction in this class of materials. It is also demonstrated that the Ru nanoparticles can undergo re-dissolution (in air at 700 °C)–exsolution cycles.

1. INTRODUCTION

A strategy to mitigate anthropogenic climate change is the capture and subsequent storage or conversion of CO_2.[1-2] In this regard, the dry reforming of methane (DRM) is a promising technology[3-5] as it converts two major greenhouse gases into a synthesis gas (Eq. 1) that can be utilized further for the synthesis of liquid fuels via the Fischer-Tropsch process.[6]

$$CH_4 + CO_2 \leftrightarrow 2CO + 2H_2 \qquad \Delta H°_{298K} = 247 \text{ kJ mol}^{-1} \qquad (1)$$

$$CH_4 \rightarrow C + 2H_2 \qquad \Delta H°_{298K} = +75 \text{ kJ mol}^{-1} \qquad (2)$$

$$2CO \leftrightarrow C + CO_2 \qquad \Delta H°_{298K} = -172 \text{ kJ mol}^{-1} \qquad (3)$$

A challenge for the industrial deployment of DRM is its high endothermicity, necessitating operating temperatures above 700 °C to yield high equilibrium conversions.[7-8] Hence, requirements for efficient DRM catalysts include a high resistance to thermal sintering and coking (by CH_4 pyrolysis, Eq. 2, and/or the disproportionation of CO, Eq. 3).[9-11] Carbon deposits may not only lead to catalyst deactivation by blocking the active sites, but could also fracture catalyst granules or lead to a high pressure drop in the reactor;[12-16] therefore, the development of DRM catalysts with a high resistance to thermal sintering and coke deposition is a key challenge.[9, 17] Several transition metals including Ni, Co, Pt, Rh, and Ru catalyze the DRM reaction[18], among them Ni-based catalysts have received appreciable attention due to their lower cost.[19-20] However, DRM catalysts based on Ni are prone to coke deposition, sintering and formation of inactive phases (with the support) with time on stream (TOS), e.g. the spinel $NiAl_2O_4$.[21-22] In contrast, DRM catalysts based on noble metals (Pt, Ru, Rh) exhibit excellent coke resistance and a higher specific activity relative to Ni-based catalysts, yet the high cost of noble metals is a disadvantage that necessitates optimal metal utilization.[23-24] Therefore it is vital to develop supported noble metal-based DRM catalysts with a minimized metal loading. The latter objective could be achieved by a high dispersion of the noble metal on a support.[25] In addition, supported nanoparticles should ideally have a uniform and controlled size and be resistant to sintering under relevant operating conditions. This is yet a challenge for noble-metal based DRM catalysts.[26-28] DRM catalysts are commonly prepared by depositing a precursor of the active metal on a metal oxide support via wetness impregnation, followed by a reduction step to form supported metal nanoparticles. However, often this method does not allow controlling the dispersion and size of the nanoparticles, and does not stabilize them against sintering with time on stream (TOS).[29-30] Approaches to reduce sintering have included a post-synthetic encapsulation or partial embedding of the active metal in a thin layer of oxides with high Tammann temperatures.[31-32] These strategies indeed improved the thermal stability of the DRM catalysts, however, at the expense of a reduced specific activity due to the partial blocking of active sites or an increased mass transfer resistance.[33-36] Recently, the so-called reductive exsolution (or reductive segregation) approach yielding highly dispersed supported metallic nanoparticles has been introduced.[37-45] This method exploits the dissolution of a late transition metal from a host oxide structure in an H_2 atmosphere and is typically applied to substituted perovskite ABO_3 phases, where a late transition metal replaces the B site metal.[38, 46] As a result, highly dispersed nanoparticles of the exsolved late transition metal can be obtained on the surface of the perovskite phase with a uniform size distribution, owing to the inherent homogeneity of the parent solid

solution oxide.[36-38, 41, 46-47] An interesting feature of exsolved nanoparticles is their socketing in the perovskite surface, a manifestation of a strong interaction between the metal and the oxide support that could reduce the mobility of the active metal under harsh reaction conditions and limit sintering of the active phase.[17, 43, 48] Importantly, investigations by transmission electron microscopy of the metal phases, reductively exsolved from substituted perovskites, suggest that the entrapment of metallic nanoparticles in the bulk of a host material is a viable scenario, and it should be minimized or avoided to make all exsolved metal accessible for gas-phase catalysis.[49-50] To date, mostly perovskite structures have been utilized for the reductive exsolution while other crystalline oxides, such as ceria-based materials with fluorite-related structures have remained underexplored.[51-53] In general, these fluorite-related structures possess a high thermal stability, oxygen ion mobility, redox activity and contain oxygen vacancies, i.e., characteristics that are advantageous for DRM catalysts.[18, 54-56] CeO_2 crystallizes in a fluorite structure (F-type) with a face centered unit cell (*Fm-3m* space group) and forms solid solutions with a large variety of metal oxides. In addition, it is capable of accommodating a high concentration of lattice defects.[57-58] Depending on the composition, solid solutions based on CeO_2 can exhibit a complex defect structure and form superstructure phases, for instance the C-type (*Ia-3*) solid solutions featuring ordered ion vacancies or pyrochlore (*Fd-3m*) phases that show a characteristic ordering of the cation sites and anion vacancies (Figure 1).[51, 59-61] As a consequence, the lattice parameter of C-type and pyrochlore structures is twice as large as that of the fluorite.

Here, we report that the reductive exsolution of Ru from defective fluorite-type solid solutions $Sm_2Ru_xCe_{2-x}O_7$ (x = 0, 0.1, 0.2, 0.4) forms highly dispersed supported Ru(0) nanoparticles (NPs, ca. 1-2 nm in diameter) that are highly active in DRM while featuring an exceptional resistivity against coking and sintering of the active phase. After 100 h TOS at 700 °C, the catalysts deactivate by only ca. 1 %. On the other hand, the benchmark catalysts prepared by wetness impregnation and sodium borohydride reduction displayed an inferior stability losing, respectively, ca. 8 and 12 % of the initial activity after only 48 h TOS. The structural evolution of the prepared materials was studied by X-ray diffraction (XRD), X-ray absorption spectroscopy (XAS), Raman spectroscopy, and transmission electron microscopy (TEM). Combined XAS-XRD experiment revealed that the exsolution of Ru(0) NPs from the $Sm_2Ru_{0.2}Ce_{1.8}O_7$ solid solution is accompanied by the transformation of the defective fluorite to a cubic C-type structure due to a rearrangement of the oxygen vacancies within the crystal lattice. Using Ru K-edge XAS analysis, we demonstrate that Ru exsolution and dissolution in reducing and oxidizing atmospheres, respectively, is a reversible process, whereby the original structure can be restored by the reincorporation of the exsolved Ru via air oxidation.

2. EXPERIMENTAL SECTION

2.1. Materials. $Ce(NO_3)_3{\cdot}6H_2O$, $Sm(NO_3)_3{\cdot}6H_2O$, RuO_2 and Pluronic P123 ($EO_{20}PO_{70}EO_{20}$; M_n ca. 5,800) were purchased from Sigma-Aldrich. Ruthenium(III) nitrosyl nitrate solution and $NaBH_4$ were purchased from Acros Organics.

2.2. Catalyst synthesis. A series of $Sm_2Ru_xCe_{2-x}O_7$–type materials with x = 0, 0.1, 0.2, 0.4 were synthesized by a gel-combustion approach.[62-63] In a typical experiment, Pluronic P123 (2 g) was dissolved in ethanol (40 mL) and the nitrates of Sm, Ce and ruthenium(III) nitrosyl nitrate were added in the desired nominal stoichiometry (3.2 mmol scale). After stirring at room temperature for 1 h, the resulting mixture was heated up to 85 °C forming a gel that was subsequently dried at 120 °C (24 h), ground, combusted at 200 °C and calcined at 800 °C (3 h).

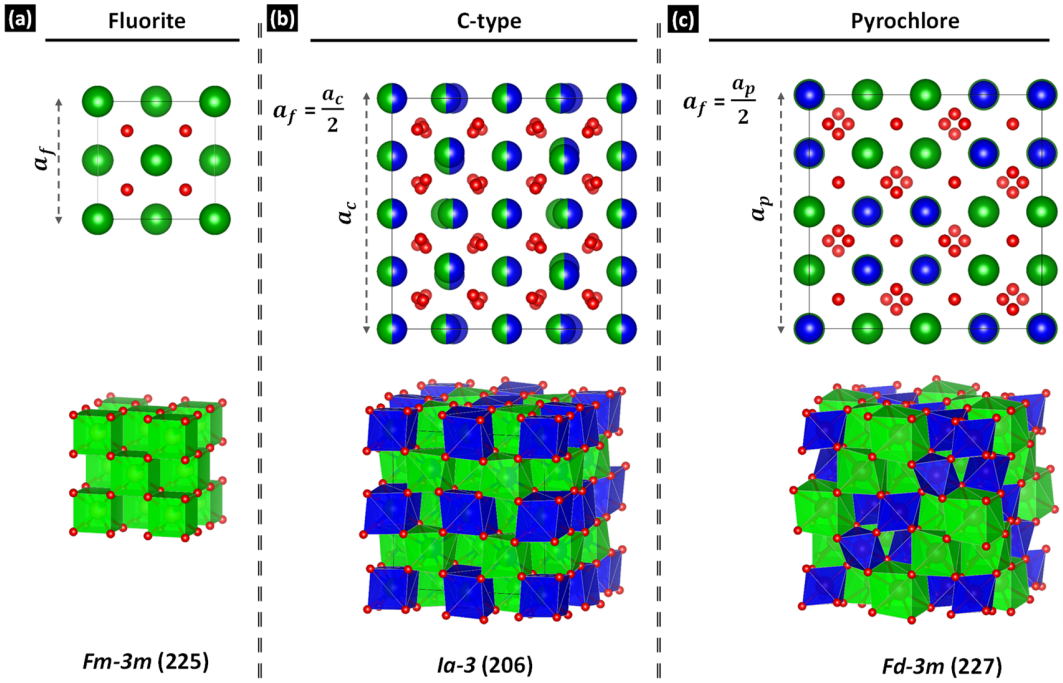

Figure 1. Schematic of the unit cell and coordination polyhedra in (a) non-defective fluorite (*Fm-3m*; Ce at 4a and O at 8c sites) (b) C type-based solid solutions, (*Ia-3*, two cations sites: 24d and 8b occupied by both Ce and lanthanides atoms statistically disordered, two oxygen sites at 48e and 16c, with oxygen vacancies preferentially located at 16c) and (c) pyrochlore structure (*Fd-3m*, $A_2B_2O_7$, A at 16d B at 16c and O at 8b and 48f sites).

Benchmark catalysts with 3 wt.% Ru loading (i.e., similar loading to that of $Sm_2Ru_{0.2}Ce_{1.8}O_7$) were prepared by wetness impregnation and sodium borohydride reduction. For the wetness impregnation method, a $Sm_2Ce_2O_7$ support, prepared as described above, was impregnated with an appropriate amount of ruthenium(III) nitrosyl nitrate solution. The resulting slurry was dried overnight at 85 °C and calcined at 800 °C (3 h) to give Ru/$Sm_2Ce_2O_7$-Imp. For the sodium borohydride reduction method, calcined $Sm_2Ce_2O_7$ (0.485 g) was stirred in a mixture of 20 mL DI water and ruthenium(III) nitrosyl nitrate solution (1 g) at room temperature for 1 h. Subsequently, under intensive stirring, 10 mL of a 0.3 M $NaBH_4$ solution in an ethanol-water (1:1) mixture was slowly added and the mixture stirred at room temperature for another hour. The resulting material was filtered, washed with DI water and dried overnight at 85 °C to give Ru/$Sm_2Ce_2O_7$-BH. Reference materials for XAS measurements were prepared by wetness impregnation (RuO_2/CeO_2) and gel-combustion ($Sm_2Ru_2O_7$). RuO_2/CeO_2 was calcined at 800 °C (3 h) while $Sm_2Ru_2O_7$ was calcined at 1050 °C (5 h).

2.3. Materials Characterization.

2.3.1. X-ray powder diffraction. Laboratory-based X-ray powder diffraction (XRD) data were collected using a PANalytical Empyrean X-ray powder diffractometer with Cu Kα X-ray radiation, operated at 45 kV and 40 mA and equipped with a X'Celerator Scientific ultra-fast line detector and a Bragg-Brentano HD incident beam optics. The scans were performed in the 2θ range of 5-90° with a step size of 0.02° and a scan speed of 0.02° s^{-1}. Additionally, synchrotron XRD data were collected at the Swiss-Norwegian beamline (SNBL, BM01A) of the European Synchrotron Radiation Facility (ESRF, Grenoble, France) using a 2M Pilatus area detector and monochromatic radiation (λ = 0.78956 Å) selected by two Rh-coated mirrors and a silicon (111) double crystal monochromator.[64] Measurements were performed in a 0.3 mm borosilicate capillary. NIST SRM660b lanthanum hexaboride was used for calibration of the wavelength and azimuthal integration. Rietveld analysis of the XRD patterns was performed using FullProf.[65]

2.3.2. In situ XAS-XRD experiments. Combined in situ XAS and powder XRD measurements were performed at BM31 (SNBL, ESRF).[66] XAS spectra were collected at the Ru K-edge using a Si(111) double crystal monochromator in transmission mode, with continuous scanning between 21950 and 22800 eV using a step size of 0.5 eV, with a total acquisition time of 150 s per scan. XRD data were collected with a 2D DEXELA detector (averaging time 30 s) using a Si (111) channel-cut monochromator set at λ=0.49328 Å.[67] The data averaging and azimuthal integration were performed using the pyFAI software and the NIST LaB_6 powder as a standard.[68] The beam size was set by slits in the horizontal and vertical directions to 0.5 mm × 2 mm for XAS and 0.5 mm × 0.5 mm for XRD measurements. Approximately 2 mg of a fresh material was placed between two plugs of quartz wool in a 1.5 mm diameter quartz capillary cell. The sample temperature was measured by placing a thermocouple (K-type) inside the catalyst bed in a separate experiment, providing a temperature calibration curve that relates the temperature inside the capillary with that of the heat blower. The materials were reduced first in 10% H_2 in He (10 mL min^{-1}) at 700 °C (10 °C min^{-1}), followed by a DRM test (CH_4 : CO_2 : He = 3 : 3 : 3 mL min^{-1}) at 700 °C. The off-gases were analysed by online mass spectrometry (MS). The cyclic reversibility of the exsolution–dissolution process was probed isothermally at 700 °C using 10% H_2/He (1 h, 10 mL min^{-1}) for reduction and 20 vol% O_2/He (1 h, 10 mL min^{-1}) for re-oxidation. In total, two reduction and re-oxidation cycles were performed and, in each cycle, XANES (X-ray absorption near edge structure) spectra and XRD data were collected for both the reduced and re-oxidized states.

2.3.3. Ex situ XAS experiments. Ex situ exsolution-dissolution experiments were performed by exposing the samples at 800 °C to a DRM reaction mixture for 1 h (i.e., CH_4 : CO_2 : N_2 = 15 : 15 : 20 mL min^{-1}) and subsequently re-oxidizing either in air (20 vol% O_2/N_2), pure CO_2, or a mixture of steam and CO_2 (10 vol% H_2O) for 1 h at different temperatures in a fixed-bed quartz reactor (400 mm length, 12.6 mm internal diameter). After each treatment, the materials were cooled down in the same stream that was used for re-oxidation. The respective re-oxidized materials were then pressed into pellets after mixing with the optimal amount of cellulose for XAS transmission measurements. For each sample, a XAS Ru K-edge spectrum was collected between 21900 and 23100 eV. Bulk RuO_2 and Ru(0) foil were used as XAS references. The XAS energy calibration was performed using a Ru(0) foil (absorption edge 22117 eV). Sm and Ce K-edge spectra were collected for the as prepared (calcined) materials at MB31, ESRF in transmission mode, using the Si(111) double crystal monochromator. The spectra were acquired between 40250-41300 eV (Ce K-edge) and 46600-48000 (Sm K-edge) with a step size of 1 eV. The processing and fitting of the extended X-ray absorption fine structure (EXAFS) data were performed using the Athena and Artemis software, respectively.[69]

2.3.4. H_2-Temperature-programmed desorption. H_2-TPD experiments were performed using an Autochem 2920 (Micromeritics) equipped with a thermal conductivity detector (TCD). For each H_2-TPD measurement, the catalyst (ca. 50 mg) was reduced at 700 °C in 5 vol% H_2/Ar for 1 h followed by an Ar purge at the same temperature for 30 min. Subsequently, the reduced sample was cooled down to 25 °C for the adsorption of H_2 (30 min). Finally, the sample was heated up to 800 °C (10 °C min^{-1}) in Ar (50 ml min^{-1}) while monitoring the desorption of H_2. The dispersion of Ru (D_{Ru}) was calculated using the volume of chemisorbed H_2 via the following equation:[70]

$$D_{Ru}\,[\%] = \frac{\text{Total number of Ru surface sites}}{\text{Total number of Ru sites}} = \left(\frac{SF \times n_{H_2} \times M_{Ru}}{w_{Ru}}\right) \times 100$$

and the particle size of Ru (d_{Ru}) was estimated assuming hemispherical particles via:

$$d_{Ru}\,(nm) = \frac{6 \times M_{Ru}}{\rho_{Ru} \times a_{Ru} \times N_A \times D_{Ru}}$$

where SF is the stoichiometric factor (Ru/H = 1.0)[71]; n_{H_2} is the quantity of adsorbed H_2 (μmol/g_{cat}) as determined by H_2-TPD; M_{Ru} is the molecular weight of Ru (101.07 g mol^{-1}); w_{Ru} is the weight fraction of Ru in the catalyst; ρ_{Ru} is the density of Ru 12.45 g cm^{-3}); a_{Ru} is the cross-sectional area of the Ru atom (6.13×10^{-20} m^2) and N_A is the Avogadro constant (6.023×10^{23} atoms mol^{-1}).

2.3.5. Raman spectroscopy. Raman spectra were recorded using a Thermo Scientific Raman spectrometer in the range 100–1500 cm^{-1} using an argon laser for excitation (wavelength 455 and 514 nm). The laser power was 4 mW and the spectral resolution was 4 cm^{-1}.

2.3.6. Transmission electron microscopy. TEM data were collected on a FEI Talos F200X equipped with a high-brightness field emission gun, a high-angle annular dark field (HAADF) detector, and a large collection-angle EDX detector. The operation voltage was set to 200 kV in both TEM and Scanning transmission electron microscopy (STEM) modes. Copper grids coated with Lacey carbon were used.

2.4. Catalytic test. DRM tests were carried out at atmospheric pressure in a fixed-bed quartz reactor (400 mm length, 12.6 mm internal diameter). In a typical experiment, 25-50 mg (depending on the gas space velocity, SV) of the calcined material was used. The total flow rate of the feed gas was set to 50 mL min^{-1} for experiments with a SV of 60 L g_{cat}^{-1} h^{-1} and 120 mL min^{-1} for a SV of

144 and 288 L g_{cat}^{-1} h^{-1} (CH_4 : CO_2 : N_2 = 50 mL min^{-1} : 50 mL min^{-1} : 20 mL min^{-1}). Prior to the activity tests, the materials were reduced in situ at 800 °C for 1 h using a DRM reaction mixture. The composition of the off-gas was analysed via a PerkinElmer Clarus 580 GC equipped with thermal conductivity and flame ionization detectors.

3. RESULTS AND DISCUSSION

3.1. Characterization of Calcined Materials. A series of $Sm_2Ru_xCe_{2-x}O_7$ (x = 0, 0.1, 0.2, 0.4) materials was prepared by a gel-combustion method (see catalyst synthesis for details). Since the exsolution method relies on a homogeneous incorporation of Ru cations into the host oxide lattice (solid solution), the structure of the calcined materials was characterized in detail by XRD, XAS and Raman spectroscopy. XRD analysis shows that, in line with previous studies,[72-73] $Sm_2Ce_2O_7$ (i.e., $Sm_2Ru_xCe_{2-x}O_7$ with x = 0) exhibits a C-type structure (Figures 1, 2a and S1). The C-type phase is a superstructure of the fluorite-type structure[60] due to an ordering of the oxygen vacancies. The C-type phase can be distinguished from the fluorite-type structure by the appearance of additional low intensity peaks in the XRD data (Figure 2a) owing to its superstructure (both C-type and fluorite phases exhibit similar main Bragg reflections). We observe that the superstructure peaks decrease in intensity upon Ru substitution in $Sm_2Ce_2O_7$ (Figure 2a, inset). For instance, comparison of the diffractograms of $Sm_2Ce_2O_7$ with that of $Sm_2Ru_{0.2}Ce_{1.8}O_7$ shows that the superstructure peaks of the former phase are replaced almost entirely by a broad diffuse scattering feature at the respective position in the diffractogram of $Sm_2Ru_{0.2}Ce_{1.8}O_7$. Rietveld refinement of the XRD data indicates that $Sm_2Ru_{0.2}Ce_{1.8}O_7$ and $Sm_2Ce_2O_7$ can be described as defective fluorite and C-type structures, with cell parameters of, respectively, a_f = 5.4619(1) and a_c = 10.9271(1) Å (Figure S3). Altogether, these XRD results demonstrate that upon incorporation of Ru into the host structure, the host C-type structure transforms into a more defective phase with disordered positions of oxygen vacancies.[74-76] The refined cell parameters of the different $Sm_2Ru_xCe_{2-x}O_7$ solid solutions are summarized in Table S1. For comparison, the cell parameters are reported based on a fluorite type unit cell, while a_f is defined as one-half of the C-type cell parameter (Figure 1).[77] We can observe only a slight decrease (<0.005 Å) in the cell parameter (a_f) of $Sm_2Ru_xCe_{2-x}O_7$ with respect to $Sm_2Ce_2O_7$. This result is in line with previous studies reporting a slight decrease in the cell parameter of CeO_2 when doping it with Ru.[78-79] Thus, the incorporation of Ru into the $Sm_2Ce_2O_7$ lattice does not lead to a considerable contraction of the unit cell (ionic radii of Ru^{4+} and Ce^{4+} are 76.0 and 111.0 Å, respectively), instead it results in a structural rearrangement of the oxygen vacancies leading to a defective fluorite type phase. On the other hand, the reference Ru/$Sm_2Ce_2O_7$-Imp material exhibits Bragg reflections ascribed to C-type $Sm_2Ce_2O_7$ and the pyrochlore phase $Sm_2Ru_2O_7$ (*Fd3m* space group). According to Rietveld refinement, the weight fraction of $Sm_2Ru_2O_7$ in Ru/$Sm_2Ce_2O_7$-Imp is ca. 6% (Figure S3c). The refined cell parameters of the $Sm_2Ru_2O_7$ and $Sm_2Ce_2O_7$ phases in Ru/$Sm_2Ce_2O_7$-Imp are a_p = 10.2704(4) Å and a_c = 10.9253(1) Å, respectively (Table S1). In contrast, the XRD pattern of the Ru/$Sm_2Ce_2O_7$-BH reference is similar to that of the $Sm_2Ce_2O_7$ support, that is no Bragg reflections related to Ru-species are observed, most likely owing to the low Ru loading and a fine dispersion of Ru on the $Sm_2Ce_2O_7$ support in Ru/$Sm_2Ce_2O_7$-BH (Figure S4a). The Raman spectra of $Sm_2Ce_2O_7$ exhibit five main bands at 190, 250, 370, 465 and 590 cm^{-1}, consistent with a C-type solid solution (Figure 2b).[72, 80-81] The band at ca. 465 cm^{-1} is characteristic for the F_{2g} symmetric vibration mode of the Ce–O bond with the Ce atom in an eightfold coordination.[60, 72] The band at ca. 590 cm^{-1} is ascribed to oxygen vacancies in the coordination sphere of Sm. A broad band of low-intensity at ca. 190 cm^{-1} is due to an oxygen vacancy surrounded by four nearest neighbouring metal atoms, while the band at ca. 370 cm^{-1} is assigned to the (A_g + F_g) symmetric stretching mode of a Sm–O bond.[60, 82] In general, the latter band at ca. 370 cm^{-1} is characteristic for C-type structures and is not observed in fluorite structures, for instance it is not found in CeO_2[82] or the reference material RuO_2 supported on CeO_2 in whichCeO_2 has a fluorite structure (RuO_2/CeO_2, Figure S4b). Similar to $Sm_2Ce_2O_7$, the five Raman bands described above are also detected in the series of $Sm_2Ru_xCe_{2-x}O_7$ (x = 0.1, 0.2, 0.4) materials (Figure S2b). Therefore, while XRD indicates that the substitution of Ce/Sm by Ru transforms the C-type structure into a fluorite phase, Raman spectroscopy suggests the presence of C-type domains within a defective fluorite phase $Sm_2Ru_xCe_{2-x}O_7$, pointing to a complex defect structure.[60, 73, 82] Increasing the fraction of Ru, we observe a red shift of the bands at 190 and 465 cm^{-1}, a reduction of the intensity of the F_{2g} band and generally a broadening of all of the bands (Figure S2b). These changes are consistent with the formation of a solid solution by the incorporation of Ru into the $Sm_2Ce_2O_7$ lattice.[56, 83] Noteworthy, a band at ca. 690 cm^{-1} is present in $Sm_2Ru_xCe_{2-x}O_7$ and Ru/$Sm_2Ce_2O_7$-Imp but is absent in $Sm_2Ce_2O_7$ (Figure 2b). While the exact nature of this band is not clear, it is likely related to the substitution of Ce/Sm by Ru cations in the host oxide lattice.[84-86]. Since the intensity of the band at ca. 690 cm^{-1} is higher in Ru/$Sm_2Ce_2O_7$-Imp compared to $Sm_2Ru_{0.2}Ce_{1.8}O_7$, and the latter material contains a $Sm_2Ru_2O_7$ phase according to XRD analysis, the band at 690 cm^{-1} might be indicative of the Sm–O–Ru environment. The absence of the 690 cm^{-1} band in the Raman spectra of the reference material Ru/$Sm_2Ce_2O_7$-BH, synthesized by a sodium borohydride reduction method, provides further support for the link between this band and the substitution of Ce or Sm cations by Ru cations in the host oxide (Figure S4c,d). It is important to note that Raman bands due to rutile RuO_2 (namely Eg, A_{1g} and B_{2g} modes at 528, 644 and 716 cm^{-1}, respectively) were not detected in either materials (455 and 514 nm lasers utilized), ruling out the presence of RuO_2.[86-87]

Next, Ru K-edge XAS analysis was employed to probe the local coordination environment around the Ru atom in $Sm_2Ru_xCe_{2-x}O_7$ and Ru/$Sm_2Ce_2O_7$-Imp. We used Ru foil, bulk rutile RuO_2, a single-phase, cubic pyrochlore $Sm_2Ru_2O_7$ and RuO_2/CeO_2 as reference materials for the analysis of the XANES and EXAFS data. Since there are no obvious differences in the XANES and EXAFS data between RuO_2/CeO_2 and RuO_2, we conclude that no solid solution between RuO_2 and CeO_2 had formed (Figure S5a-c). The normalized Ru K-edge XANES spectra and Fourier transformed EXAFS functions of $Sm_2Ru_{0.2}Ce_{1.8}O_7$ and Ru/$Sm_2Ce_2O_7$-Imp are compared with selected reference materials in Figure 2c-d. The edge position of $Sm_2Ru_{0.2}Ce_{1.8}O_7$ is close to that of RuO_2 suggesting the same +4 oxidation state of Ru (22131 and 22130 eV, respectively). However, the distinct features observed in the white line region (ca. 22125-22165 eV) of $Sm_2Ru_{0.2}Ce_{1.8}O_7$ relative to the references RuO_2 and $Sm_2Ru_2O_7$ (Figures 2c and S2) suggest a different environment of Ru in $Sm_2Ru_{0.2}Ce_{1.8}O_7$. Next, the Fourier and the wavelet transforms (FT and WT, respectively) of the EXAFS data were analyzed. The WT method allows resolving the contribution of different backscattering neighbouring atoms located at similar distances from the scattering atom.[88-89] The FT and WT of the EXAFS of RuO_2 exhibit two coordination spheres at ca. 1.6 and 3 Å, ascribed to Ru–O and Ru–Ru shells, respectively (Figure 2d and S5d). In contrast, the FT and WT (not corrected for the phase shift) for $Sm_2Ru_{0.2}Ce_{1.8}O_7$ reveal a Ru–O shell at about 1.6 Å without well-defined features at higher interatomic distances. The absence of a second coordination shell at ca. 3 Å (i.e., Ru–Ru shell)

rules out the presence of a RuO_2 phase in $Sm_2Ru_{0.2}Ce_{1.8}O_7$, in agreement with the results of the Raman spectroscopy and XRD, and suggests the full dissolution of Ru^{4+} cations into the fluorite host structure.[90-91]

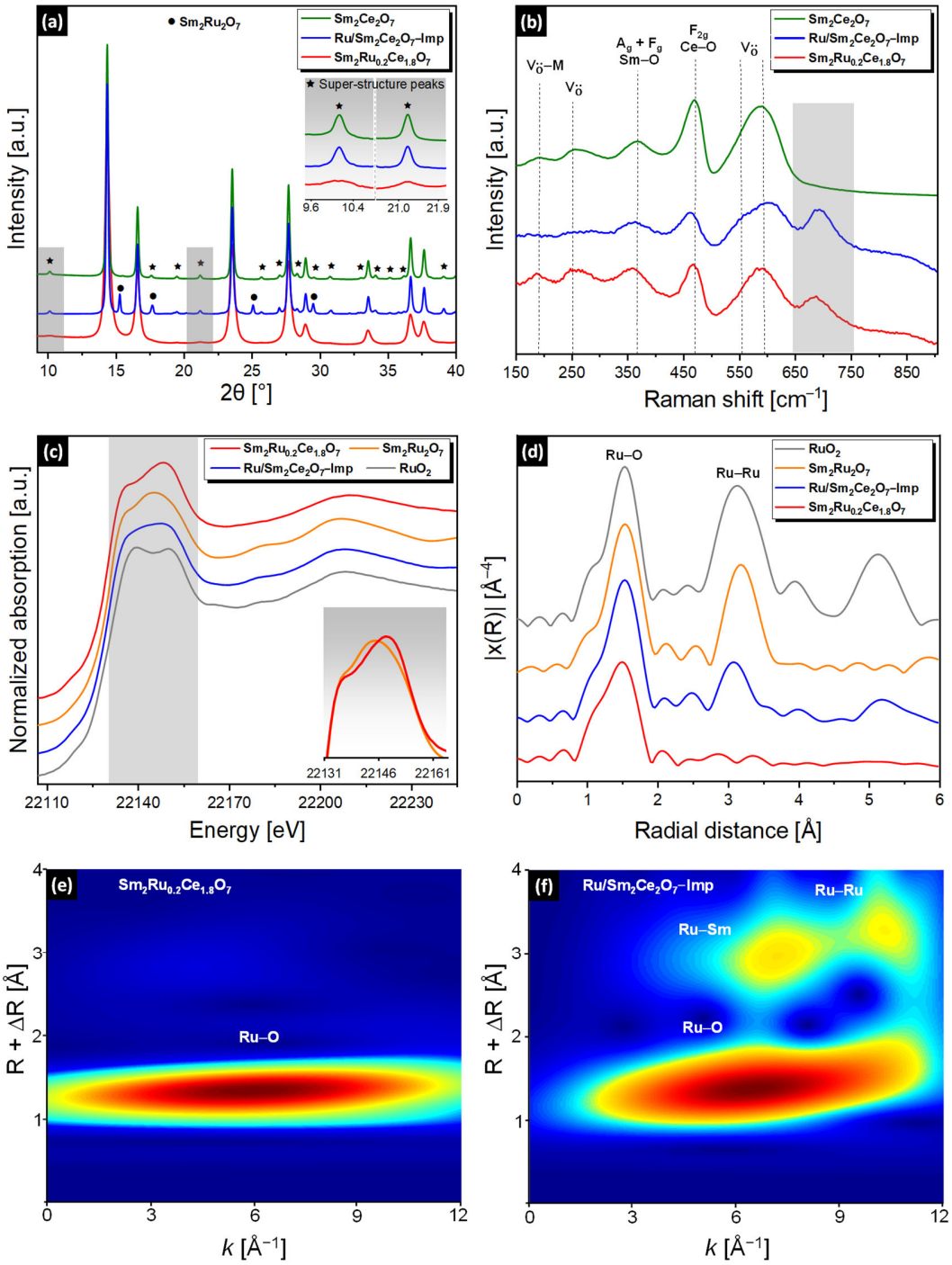

Figure 2. Comparison of the synthesized materials calcined at 800 °C: (a) XRD patterns (λ=0.78956 Å) of $Sm_2Ce_2O_7$, $Sm_2Ru_{0.2}Ce_{1.8}O_7$ and $Ru/Sm_2Ce_2O_7$-Imp. (b) Raman spectra (455 nm laser excitation) of $Sm_2Ce_2O_7$, $Ru/Sm_2Ce_2O_7$-Imp, and $Sm_2Ru_{0.2}Ce_{1.8}O_7$ with the assignment of bands ($V_{\ddot{o}}$ is an oxygen vacancy site). (c) Normalized Ru K-edge XANES spectra, (d) Fourier transforms of k^3-weighted EXAFS data, and (e, f) WT of k^3-weighted EXAFS signals for $Sm_2Ru_{0.2}Ce_{1.8}O_7$ and $Ru/Sm_2Ce_2O_7$-Imp catalysts.

Likewise, the series of $Sm_2Ru_xCe_{2-x}O_7$ (x = 0.1, 0.4) materials possess only a Ru–O shell, suggesting a similar local Ru coordination environment for varying Ru contents (Figure S2). The Ru K-edge EXAFS fitting results of $Sm_2Ru_xCe_{2-x}O_7$ (Table S2) show an average coordination number of the nearest Ru–O shell at 1.97(1) Å of 6(1). The fact that this coordination number is lower than the metal-

oxygen coordination in a perfect non-defective fluorite-type structure (8 oxygen neighbors), and lower than for the Ce–O and Sm–O path (vide infra), suggests that the oxygen vacancies in the solid solution are preferentially located adjacent to the Ru cations.[92-93] Moreover, this preferential location of oxygen vacancies in the vicinity of Ru atoms, together with the differences between the Ru–O distance and the longer Ce–O and Sm–O distances (Table S3 and vide infra) lead to a local, structural distortion around the Ru atoms. The local disorder around Ru in the $Sm_2Ru_xCe_{2-x}O_7$ solid solutions leads in turn to an unobservable second shell by Ru K-edge EXAFS (Figure 2c,d). The absence of a second shell peak in the FT-EXAFS is explained by a destructive interference of EXAFS signals of the scatters from Sm and Ce atoms located at different distances from the absorbing Ru atom (Figure 2c,d). The Ce K-edge and Sm K-edges XANES and EXAFS provided complementary information to the local structure of the $Sm_2Ru_xCe_{2-x}O_7$ solid solutions (Figure 3a-d). The corresponding FT of the Ce K-edge and Sm K-edge EXAFS are presented in Figure 3b and Figure 3d, respectively. The first peak in the FT is ascribed to the Ce–O or Sm–O shells, i.e., the nearest neighbors, while the second peak is attributed to the Ce–M or Sm–M shell, where M can be either Ce, Sm or Ru. In both Ce K-edge and Sm K-edge EXAFS spectra, a reduction in the amplitude of the FT intensity with increasing Ru loading in $Sm_2Ru_xCe_{2-x}O_7$ is observed (Figure 3b,d), which could be ascribed to an increasingly more defective crystalline lattice. This is in agreement with the XRD data that suggest a transition from an ordered C-type to the more disordered structure and is also consistent with the Ru K-edge analysis that indicates the appearance of a local disorder upon the incorporation of Ru in the structure. Previously, a reduction in the amplitude of the FT EXAFS intensities with an increasing fraction of a dopant in $Ce_{1-x}Ln_xO_2$ (Ln = Sc, Y, Nd, Sm) solid solutions was linked to a disruption of the local structure.[94,95] The structural parameters determined by the fitting of the EXAFS data at the Ru, Ce and Sm K-edges are summarized in Table S3. It is noteworthy that in all $Sm_2Ru_xCe_{2-x}O_7$ solid solutions, the Ce–O and Sm–O distances remain nearly constant at ca. 2.29(1) and 2.37(1) Å, respectively. Similar results were reported for solid solutions of the type $Ce_{1-x}Sm_xO_2$,[96] in agreement with the larger ionic radius of Sm^{3+} compared to Ce^{4+} (108 and 97 pm, respectively).[97] The solid solutions of the type $Sm_2Ru_xCe_{2-x}O_7$ feature coordination numbers between 8.3(8) and 8.4(8) for the nearest O shell surrounding Ce and between 7.1(8) and 7.8(9) for the nearest O shell surrounding Sm atoms (Table S3 and Figure S6c).

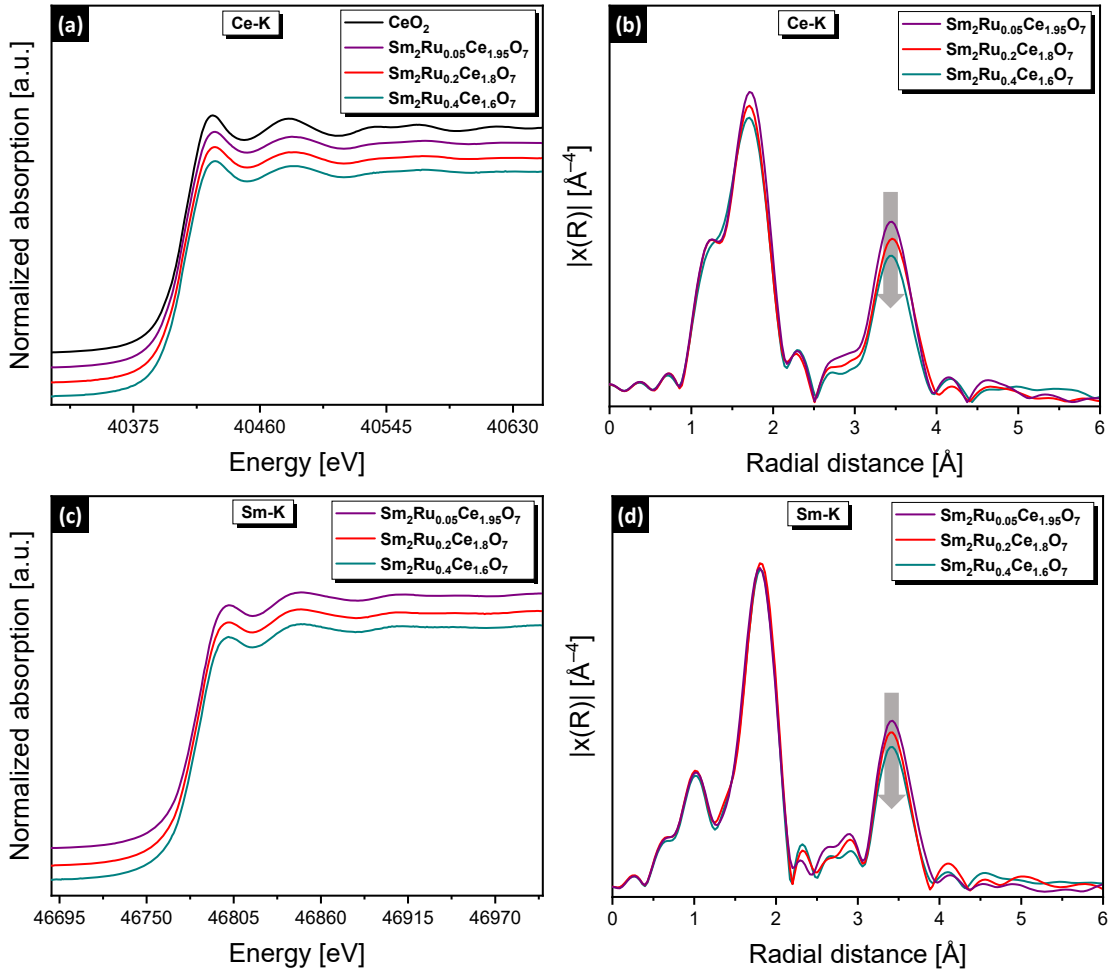

Figure 3. Normalized Ce (a, b) and Sm (c, d) K-edges XANES spectra and Fourier transforms of k^3-weighted EXAFS data for $Sm_2Ru_xCe_{2-x}O_7$ (x = 0.05, 0.2, 0.4) materials, respectively.

To summarize, the local analysis of the Ru, Sm and Ce sites highlights the formation of $Sm_2Ru_xCe_{2-x}O_7$ solid solutions that are highly defective around the Ru positions in the structure. Consistent with our XRD and Rietveld refinement results (Figures 2a and S3c), Ru/$Sm_2Ce_2O_7$-Imp shows similar XANES and EXAFS features as the reference $Sm_2Ru_2O_7$ pyrochlore phase (Figure 2c,d). According to WT EXAFS analysis, the local structure of Ru/$Sm_2Ce_2O_7$-Imp has two coordination spheres, the first is the Ru–O sphere and the second shell is composed of two subshells, Ru–Sm and Ru–Ru, confirming the formation of $Sm_2Ru_2O_7$ pyrochlore domains in Ru/$Sm_2Ce_2O_7$-Imp (Figure 2e,f). Full details of the FT-EXAFS fittings are presented in Figure S6a,b and Table S2. HR-TEM coupled with STEM-EDX analysis was applied to compare the morphology, structure and the compositional homogeneity of $Sm_2Ru_{0.2}Ce_{1.8}O_7$ and Ru/$Sm_2Ce_2O_7$-Imp. STEM-EDX confirms a high atomic dispersion of Sm and Ce in $Sm_2Ce_2O_7$ with a recorded inter-plane spacing of 0.315 nm that corresponds to the (2 2 2) plane of the $Sm_2Ce_2O_7$ lattice (Figure 4a,b). As evidenced by the lattice fringes in HR-TEM, $Sm_2Ru_{0.2}Ce_{1.8}O_7$ is highly crystalline and exhibits a homogeneous spatial distribution of Ru, Sm, and Ce (Figure 4c,d). A similar degree of crystallinity and homogeneity was also observed for Ru/$Sm_2Ce_2O_7$-Imp (Figure 4e,f).

3.2. Exsolution of Ru from $Sm_2Ru_{0.2}Ce_{1.8}O_7$ and Ru/$Sm_2Ce_2O_7$-Imp. Having established the structure of the as-prepared (calcined) materials, we probed their evolution under reductive H_2 conditions by in situ XAS (Ru K-edge) and XRD. Upon reductive treatment at 700 °C in 10 vol% H_2 in He (10 mL min^{-1}, 1 h), the absorption edge in the XANES spectra for both $Sm_2Ru_{0.2}Ce_{1.8}O_7$ and Ru/$Sm_2Ce_2O_7$-Imp shifts towards lower energies (from ca. 22131 eV in the calcined materials to 22117 eV in the reduced materials), consistent with the formation of metallic Ru (the edge position for Ru foil is at 22117 eV, Figures 5a, S7a,b).

Comparison of the Ru K-edge XANES spectra of $Sm_2Ru_{0.2}Ce_{1.8}O_7$ and Ru/$Sm_2Ce_2O_7$-Imp after the reductive treatment reveals their close match to the spectrum of the Ru foil, suggesting a complete Ru reduction (an important aspect with regards to high metal utilization). The WT of the Ru K-edge EXAFS data of $Sm_2Ru_{0.2}Ce_{1.8}O_{7(H2\text{-}700)}$ collected at 25 °C exhibit a Ru–Ru shell at about 2.5 Å confirming the exsolution of metallic Ru from the structure (Figure 5b). The XRD data show that the reductive exsolution of Ru from $Sm_2Ru_{0.2}Ce_{1.8}O_7$ induces a fluorite-to-C-type transition (Figure 5c), leading to the formation of a super-cell with ordered oxygen vacancies that are typical for $Sm_2Ce_2O_7$, as discussed above. On the other hand, the reduction of Ru/$Sm_2Ce_2O_7$-Imp leads to XRD reflections ascribed to metallic Ru. Simultaneously, peaks due to the $Sm_2Ru_2O_7$ pyrochlore phase disappear (Figure 5d). Figure S7c compares the FT EXAFS of $Sm_2Ru_{0.2}Ce_{1.8}O_7$ and Ru/$Sm_2Ce_2O_7$-Imp reduced at 700 °C, referred to as $Sm_2Ru_{0.2}Ce_{1.8}O_{7(700\text{-}H2)}$ and Ru/$Sm_2Ce_2O_7$-$Imp_{(700\text{-}H2)}$, to that of Ru foil. The amplitude of the peak related to the Ru-Ru coordination sphere in $Sm_2Ru_{0.2}Ce_{1.8}O_{7(700\text{-}H2)}$ is smaller than in Ru/$Sm_2Ce_2O_7$-$Imp_{(700\text{-}H2)}$ and the Ru foil, in agreement with the fitted Ru-Ru coordination numbers of 6(1), 10(1), 12.0, respectively (Table S2), which indicates a smaller size of the exsolved Ru(0) nanoparticles in $Sm_2Ru_{0.2}Ce_{1.8}O_{7(700\text{-}H2)}$ relative to Ru/$Sm_2Ce_2O_7$-$Imp_{(700\text{-}H2)}$. This analysis suggests the exsolution of very small (ca. 1-1.5 nm in size) Ru nanoparticles in $Sm_2Ru_{0.2}Ce_{1.8}O_{7(700\text{-}H2)}$[98-99] explaining the absence of XRD peaks due to metallic Ru in $Sm_2Ru_{0.2}Ce_{1.8}O_{7(700\text{-}H2)}$ (in contrast to Ru/$Sm_2Ce_2O_7$-$Imp_{(700\text{-}H2)}$, Figure 5c,d). To probe the cyclic reversibility of the Ru exsolution–dissolution process, we subjected $Sm_2Ru_{0.2}Ce_{1.8}O_{7(700\text{-}H2)}$ in situ to a flow of 20 vol% O_2 in He at 700 °C (isothermal conditions) and observed the re-incorporation (dissolution) of the exsolved Ru(0) back into the lattice of the host oxide and the restoration of the original structure.

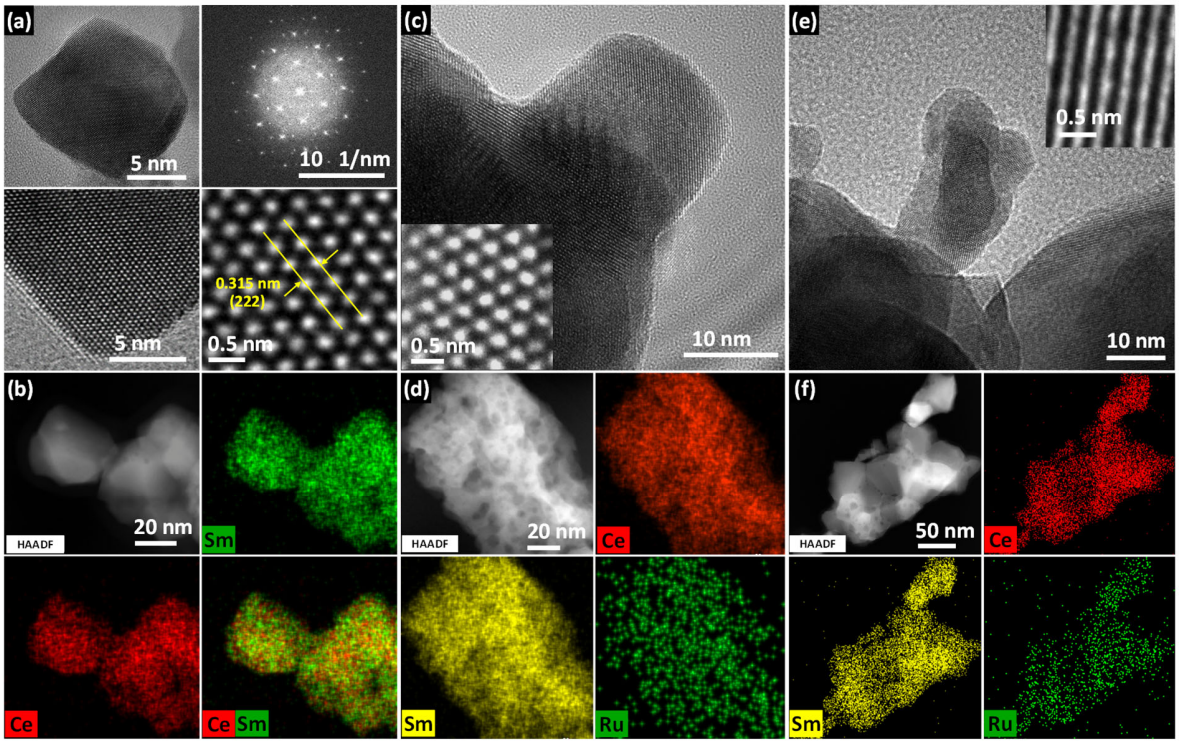

Figure 4. TEM, Selected area electron diffraction (SAED) and STEM-EDX images of calcined (a, b) $Sm_2Ce_2O_7$, (c, d) $Sm_2Ru_{0.2}Ce_{1.8}O_7$ and (e, f) Ru/$Sm_2Ce_2O_7$-Imp.

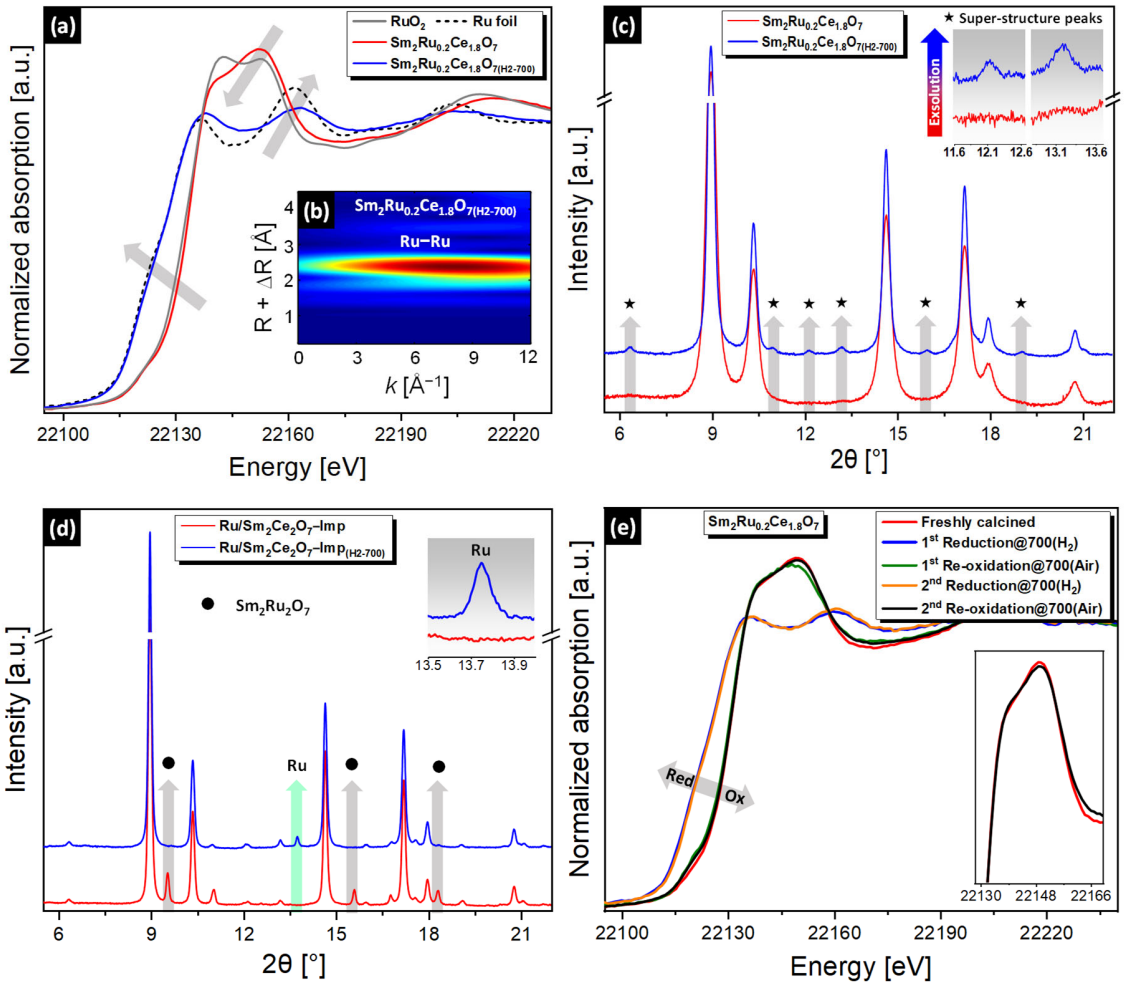

Figure 5. (a) Normalized in situ Ru K-edge XANES spectra of $Sm_2Ru_{0.2}Ce_{1.8}O_7$ before and after H_2-treatment (10 vol% H_2 in He) at 700 °C. (b) WT of the k^3-weighted EXAFS signals for $Sm_2Ru_{0.2}Ce_{1.8}O_{7(H2\text{-}700)}$. (c, d) XRD results of TPR experiments (10 vol% H_2 in He) for $Sm_2Ru_{0.2}Ce_{1.8}O_7$ and Ru/$Sm_2Ce_2O_7$-Imp (λ=0.49328 Å). (e) Normalized in situ Ru K-edge XANES spectra for $Sm_2Ru_{0.2}Ce_{1.8}O_7$ after two redox cycles at 700 °C. The reduction and re-oxidation were performed in 10 vol% H_2 in He and 20 vol% O_2 in He, respectively.

According to Ru K-edge XANES data, the dissolution of exsolved Ru(0) into the host oxide proceeded rapidly at this temperature, since the re-oxidized $Sm_2Ru_{0.2}Ce_{1.8}O_{7(700\text{-}H2)}$ material fully recovered all features of the freshly calcined material within ca. 10 minutes (Figures S6d and 2c). Next, we repeated cycles of alternating H_2 reduction for Ru exsolution (10 vol% H_2 in He) followed by air oxidation for Ru dissolution at 700 °C. Our results demonstrate that the Ru exsolution–dissolution process is reversible according to in situ Ru K-edge XANES data (Figure 5e). In line with the XANES observations, the FT EXAFS data of the re-oxidized $Sm_2Ru_{0.2}Ce_{1.8}O_{7(700\text{-}H2)}$ (collected at 25 °C) shows a peak owing to the Ru–O shell and no strong contribution from the second and third nearest neighboring coordination shells in the range 2–4 Å (Figure S7d,e), i.e., similar signatures as the initial solid solution. This excludes the presence of Ru(0) and RuO_2 phases in the re-oxidized $Sm_2Ru_{0.2}Ce_{1.8}O_{7(700\text{-}H2)}$ and highlights that Ru is re-dissolved into the host structure re-forming the original $Sm_2Ru_{0.2}Ce_{1.8}O_7$ solid solution (Figure S7d,e).[100] The EXAFS fittings confirm that the Ru–O coordination numbers for both re-oxidized $Sm_2Ru_{0.2}Ce_{1.8}O_{7(700\text{-}H2)}$ and freshly calcined $Sm_2Ru_{0.2}Ce_{1.8}O_7$ are similar, i.e., 6(1) (Table S2), highlighting the reversibility of the Ru exsolution–dissolution process. In addition, ex situ prepared $Sm_2Ru_{0.2}Ce_{1.8}O_{7(700\text{-}H2)}$ and Ru/$Sm_2Ce_2O_7$-$Imp_{(700\text{-}H2)}$ (10 vol% H_2 in N_2, 700 °C, 1 h) were characterized by TEM, STEM, and STEM-EDX (Figures 6a,b, S8a,e and S9a,b). The surface morphology of $Sm_2Ru_{0.2}Ce_{1.8}O_{7(700\text{-}H2)}$ is highly porous according to the secondary electron image that was recorded simultaneously with the HAADF-STEM image at the identical location (Figure S10). EDX elemental mapping of $Sm_2Ru_{0.2}Ce_{1.8}O_{7(700\text{-}H2)}$ shows that Sm, O, and Ce are more uniformly distributed than Ru (Figure S8e). This is in contrast with the calcined material that shows a homogeneous distribution of all elements (Figure 4d). In fact, very small Ru NPs of ca. 1.5 nm are discernible by TEM on the surface of $Sm_2Ru_{0.2}Ce_{1.8}O_{7(700\text{-}H2)}$ (Figure 6a), in agreement with the absence of reflections due to metallic Ru in XRD and the low Ru coordination number extracted from the EXAFS fittings. In contrast, poorly dispersed and larger Ru nanoparticles of ca. 4 nm are observed in Ru/$Sm_2Ce_2O_7$-$Imp_{(700\text{-}H2)}$ (Figure S9a,b). Subsequently, H_2-TPD measurements were employed to compare the specific Ru dispersion and the particle size to the sizes obtained from XAS and TEM measurements. H_2-TPD data show a significantly higher Ru dispersion for $Sm_2Ru_{0.2}Ce_{1.8}O_{7(700\text{-}H2)}$ relative to Ru/$Sm_2Ce_2O_7$-$Imp_{(700\text{-}H2)}$, i.e., 65 and 26 %, respectively (Table S4). Accordingly, the average particle size of Ru(0) in

$Sm_2Ru_{0.2}Ce_{1.8}O_{7(700\text{-}H2)}$ is smaller than that in $Ru/Sm_2Ce_2O_7\text{-}Imp_{(700\text{-}H2)}$, i.e., ca. 2 and 5 nm, respectively, as determined by H_2-TPD, which is in reasonable agreement with TEM and XAS measurements. Based on these results, we conclude that the reductive exsolution of Ru from $Sm_2Ru_{0.2}Ce_{1.8}O_7$ solid solution yields highly dispersed supported Ru(0) NPs of ca. 1-2 nm in diameter on the surface of C-type $Sm_2Ce_{1.8}O_{7-\delta}$ and does not form Ru(0) NPs in the bulk of the $Sm_2Ce_{1.8}O_{7-\delta}$ support.

3.3. Active structure under DRM conditions and catalytic performance. In order to determine whether $Ru/Sm_2Ce_2O_7\text{-}Imp_{(700\text{-}H2)}$ and $Sm_2Ru_{0.2}Ce_{1.8}O_{7(700\text{-}H2)}$ evolve structurally under DRM conditions with TOS, alternating XRD and XAS (Ru K-edge) data were collected under operando DRM conditions in a quartz capillary reactor (700 °C, 2 h, SV = 270 L g_{cat}^{-1} h^{-1}). The off-gas composition was monitored by a mass spectrometer (Figure S11). For both catalysts, the main products under DRM conditions were H_2, CO, and H_2O and no other carbon-containing side products were detected. Interestingly, no apparent deactivation was observed in the operando XAS experiment within 2 h TOS for both catalysts at 700 °C. Operando XANES (Figure S12a,d) results reveal no noticeable structural changes under DRM conditions compared to reduced $Sm_2Ru_{0.2}Ce_{1.8}O_{7(700\text{-}H2)}$, also revealing that the C-type support structure is preserved under reactive conditions according to XRD (Figure S12b,e). However, FT EXAFS results uncover a small rise in the amplitude of the Ru-Ru coordination peak and the respective coordination number at the end of the operando DRM test (labelled as post-DRM, Figure S12c,f). The coordination number of Ru increased from 10(1) to 11(1) for $Ru/Sm_2Ce_2O_7\text{-}Imp_{(700\text{-}H2)}$ and from 6(1) to 7(1) for $Sm_2Ru_{0.2}Ce_{1.8}O_{7(700\text{-}H2)}$ (Table S2). This increase can be attributed to the growth of the Ru NPs with TOS.

Next, we assessed if Ru exsolution could proceed also under DRM conditions (hence, alleviating the need for the H_2 pre-treatment step). To this end, we exposed calcined $Sm_2Ru_{0.2}Ce_{1.8}O_7$ to DRM conditions at 800 °C for 1 h and collected ex situ Ru K-edge XAS and XRD data of the resulting $Sm_2Ru_{0.2}Ce_{1.8}O_{7(800\text{-}DRM)}$ material (Figures S13a-b and S13c, respectively). In the XANES region, the identical absorption edge position and the white-line feature of the reference Ru foil and $Sm_2Ru_{0.2}Ce_{1.8}O_{7(800\text{-}DRM)}$ reveal that Ru exsolves indeed under DRM conditions, forming metallic Ru nanoparticles (Figure S13a). Figure S13b compares the FT EXAFS function of $Sm_2Ru_{0.2}Ce_{1.8}O_{7(800\text{-}DRM)}$ with the reference Ru foil. Expectedly, similar to $Sm_2Ru_{0.2}Ce_{1.8}O_{7(700\text{-}H2)}$ (Figure S7c), the amplitude of the peak related to the Ru-Ru coordination sphere in $Sm_2Ru_{0.2}Ce_{1.8}O_{7(800\text{-}DRM)}$ is smaller than in the Ru foil. EXAFS fittings reveal that the Ru-Ru coordination numbers for both $Sm_2Ru_{0.2}Ce_{1.8}O_{7(800\text{-}DRM)}$ and $Sm_2Ru_{0.2}Ce_{1.8}O_{7(700\text{-}H2)}$ are comparable (i.e., 6.6 and 6.1, respectively, Table S2), highlighting the exsolution of Ru nanoparticles of similar size (ca. 1-2 nm) under these conditions. Additionally, similar to the exsolution experiments in a H_2 atmosphere, superstructure peaks appear in the XRD pattern of $Sm_2Ru_{0.2}Ce_{1.8}O_{7(800\text{-}DRM)}$ (Figure S13c,d). These results indicate a very similar structural evolution of $Sm_2Ru_{0.2}Ce_{1.8}O_7$ upon H_2-reduction at 700 °C or treatment under DRM conditions at 800 °C. We speculate that H_2 and possibly CO produced under DRM conditions on surface Ru sites are responsible for the exsolution of Ru nanoparticles from $Sm_2Ru_{0.2}Ce_{1.8}O_7$.

The catalytic activity and stability of the prepared Ru-based materials for the DRM (Eq. 1) was evaluated further in a fixed bed reactor at 700 °C under atmospheric pressure (SV = 60 L g_{cat}^{-1} h^{-1}) for 48 h time on stream. Prior to acquiring the activity data, the materials were treated in situ with a DRM reaction mixture for 1 h at 800 °C. $Sm_2Ru_{0.2}Ce_{1.8}O_7$, $Ru/Sm_2Ce_2O_7$-Imp as well as an additional reference catalyst $Ru/Sm_2Ce_2O_7$-BH (see Figure S4b,c for characterization data of this material) yielded a nearly identical initial conversion of methane of ca. 70 % (Figure 7a). However, $Ru/Sm_2Ce_2O_7$-BH deactivated with the fastest rate reaching a plateau at ca. 62 % conversion after 48 h of TOS (12 % drop). $Ru/Sm_2Ce_2O_7$-Imp deactivated to a lesser extent. The CH_4 conversion decreased by only 8 % over 48 h TOS. The highest catalytic activity and stability was observed for $Sm_2Ru_{0.2}Ce_{1.8}O_7$ maintaining a stable 69 % CH_4 conversion throughout 48 h. Further catalytic tests of $Sm_2Ru_{0.2}Ce_{1.8}O_7$ assessed the dependence of the catalyst's stability on the space velocity (24 h TOS at 700 °C) and temperature (Figure 7b,c). A nearly constant CH_4 conversion was observed at a high SV of 288 L g_{cat}^{-1} h^{-1} (Figure 7b). The long-term stability of $Sm_2Ru_{0.2}Ce_{1.8}O_7$ was confirmed further at 700 °C for ca. 105 h TOS (SV 60 L g_{cat}^{-1} h^{-1}) with the catalyst not showing any signs of deactivation (Figure S14).

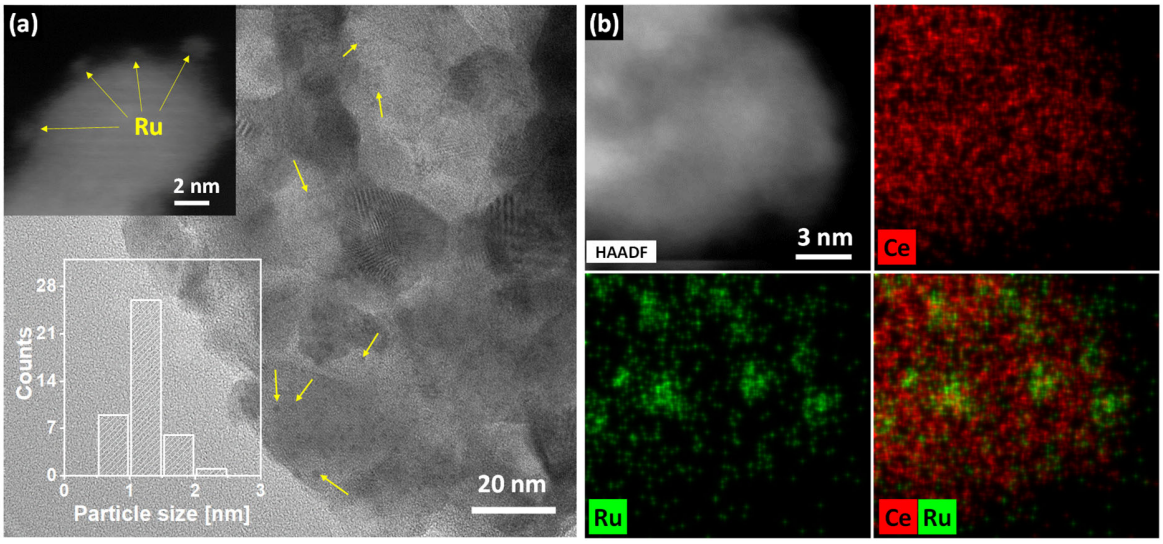

Figure 6. (a, b) TEM and STEM-EDX images of the ex situ prepared (10 vol% H_2, 700 °C, 1 h) $Sm_2Ru_{0.2}Ce_{1.8}O_{7(700\text{-}H2)}$.

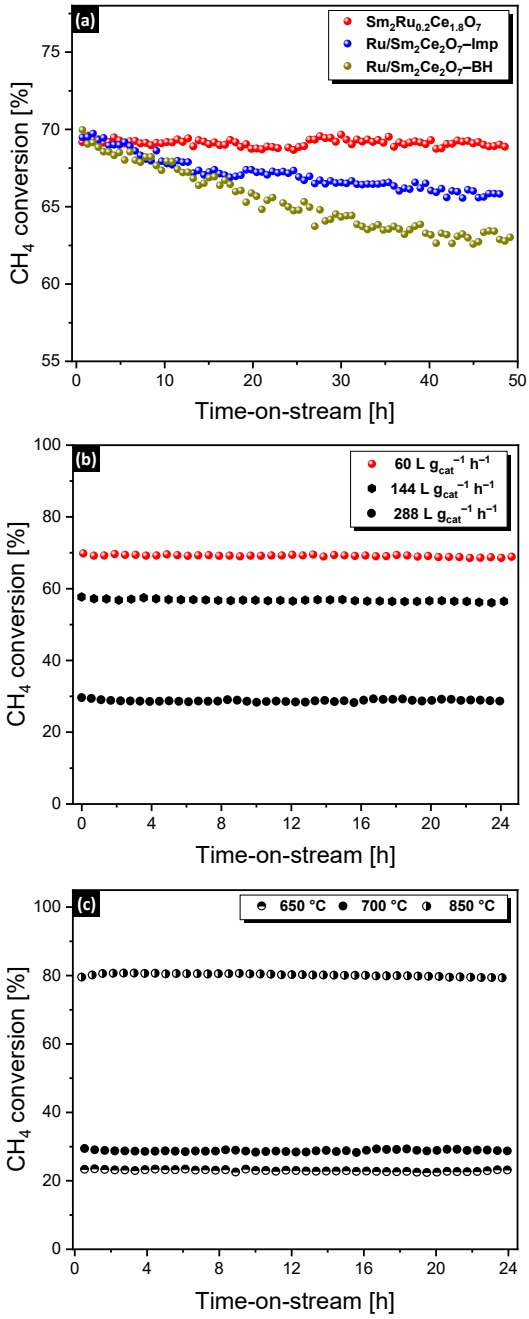

Figure 7. (a) CH_4 conversions versus time on stream for $Sm_2Ru_{0.2}Ce_{1.8}O_7$, Ru/$Sm_2Ce_2O_7$-Imp and Ru/$Sm_2Ce_2O_7$-BH (700 °C, SV = 60 L g_{cat}^{-1} h^{-1}). (b, c) Effect of SV and reaction temperature on the catalytic performance of $Sm_2Ru_{0.2}Ce_{1.8}O_7$. Prior to acquiring activity data, each catalyst was treated under the DRM reaction mixture for 1 h at 800 °C.

We note that for all of the space velocities tested here and independent of the catalyst, the CO_2 conversion was greater than the CH_4 conversion due to the competing reverse water gas shift reaction (RWGS, Eq. 4, Figures S15a and S16a) giving a H_2/CO ratio of ca. 0.85, 0.83 and 0.86 for $Sm_2Ru_{0.2}Ce_{1.8}O_7$, Ru/$Sm_2Ce_2O_7$-Imp and Ru/$Sm_2Ce_2O_7$-BH catalysts, respectively.

$$CO_2 + H_2 \leftrightarrow CO + H_2O \quad \Delta H°_{298K} = +41.2 \text{ kJ mol}^{-1} \qquad (4)$$

Our experiments show also that the stability of $Sm_2Ru_{0.2}Ce_{1.8}O_7$ is maintained at higher temperatures, viz. 850 °C and a higher SV of 288 L g_{cat}^{-1} h^{-1} during a 24 h TOS test (Figures 7c and S15b, 80 and 89 % conversions of CH_4 and CO_2, respectively). In line with the endothermicity of the DRM reaction, the conversion of methane is decreased to 23 % at 650 °C (Figure 7c), yet the lower temperature did not affect the stability of the catalyst. Next, we assessed the impact of the Ru loading in $Sm_2Ru_xCe_{2-x}O_7$ (x = 0.1, 0.2, 0.4) on the catalytic performance and found that all $Sm_2Ru_xCe_{2-x}O_7$ materials provided a stable activity over 24 h TOS (Figure S17). Expectedly, the conversions of CH_4 and CO_2 increased with increasing Ru loading in the catalyst. An Arrhenius plot reveals an apparent activation energy (E_a) of ca. 73 kJ mol^{-1} for $Sm_2Ru_{0.2}Ce_{1.8}O_7$ (Figure S16b), comparable with other Ru-based catalysts.[101] In summary, our DRM tests, including those at high temperature and space velocity, demonstrate an excellent performance and in particular stability of $Sm_2Ru_xCe_{2-x}O_7$, independent of the Ru loading, highlighting that reductive exsolution leads to active and highly stable Ru-based DRM catalysts. Analysis of $Sm_2Ru_{0.2}Ce_{1.8}O_7$ after the DRM reaction (laboratory experiment, 700 °C, 48 h TOS, SV = 60 L g_{cat}^{-1} h^{-1}) by HR-TEM and STEM shows that the reacted material contains exsolved Ru nanoparticles of an average size of ca. 2.2 nm (Figure 8a,b), somewhat larger compared to those in $Sm_2Ru_{0.2}Ce_{1.8}O_{7(700\text{-}H2)}$. After the catalytic test, the exsolved nanoparticles appear partially embedded (socketed)[36] into the parent oxide surface (Figure 8b). Increasing the DRM reaction temperature to 800 °C while keeping the other parameters constant, gives slightly larger Ru particles of ca. 2.7 nm for $Sm_2Ru_{0.2}Ce_{1.8}O_7$ catalyst, albeit still being highly-dispersed on the oxide surface according to TEM (Figure 8c,d). This slight increase of the particle size occurs while preserving the high dispersion of the Ru NPs on the support, hence pointing to Ostwald ripening as the main sintering mechanism (via Ru clusters < 1 nm in size that are not detectable by HR-TEM). The high dispersion of the exsolved Ru NPs is also maintained in $Sm_2Ru_{0.2}Ce_{1.8}O_7$ after the extended stability test (105 h, Figure S18a). Similar observations were made for the catalyst with the high Ru loading, i.e., $Sm_2Ru_{0.4}Ce_{1.6}O_7$ (Figure S19). This contrasts with what is observed for spent Ru/$Sm_2Ce_2O_7$-Imp and Ru/$Sm_2Ce_2O_7$-BH. Already after 48 h TOS (at 700 °C), a significant sintering-induced growth of the Ru nanoparticles was observed in these materials (Figures S9c and S18b), which correlates well with their deactivation with TOS (Figure 7a). Overall, electron microscopy and operando XAS study point to an increased resistance of Ru NPs against sintering with TOS as a key factor to explain the superior stability of the exsolved catalysts compared to the references Ru/$Sm_2Ce_2O_7$-Imp and Ru/$Sm_2Ce_2O_7$-BH.

3.4. Reversibility of Ru exsolution. Metal exsolution from and reincorporation back into the host oxide lattices (dissolution) is a temperature-dependent process.[40] To further understand the dissolution process, we treated $Sm_2Ru_{0.2}Ce_{1.8}O_{7(800\text{-}DRM)}$ in air (1 h, 50 mL min^{-1}, SV = 60 L g_{cat}^{-1} h^{-1}) isothermally at 400, 500, 700 and 800 °C while determining the reincorporation of Ru by ex situ XANES, EXAFS, Raman spectroscopy and XRD (Figure 9). Each re-oxidation at a given temperature was performed with a fresh material of $Sm_2Ru_{0.2}Ce_{1.8}O_{7(800\text{-}DRM)}$. As already discussed above, the edge position of Ru in $Sm_2Ru_{0.2}Ce_{1.8}O_{7(800\text{-}DRM)}$ is identical to that of Ru foil, suggesting that Ru is in a metallic state. Subjecting $Sm_2Ru_{0.2}Ce_{1.8}O_{7(800\text{-}DRM)}$ to air at 400 °C already gives an average oxidation state of Ru that is close to that in the calcined material.

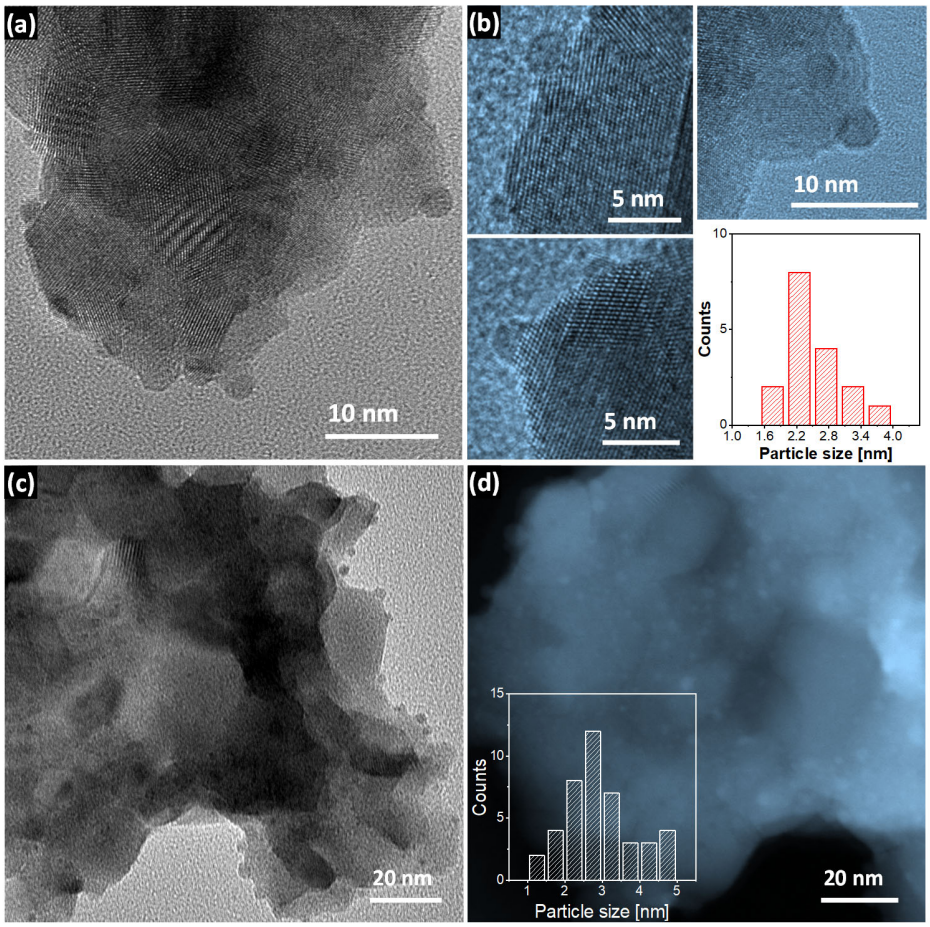

Figure 8. TEM and STEM images of $Sm_2Ru_{0.2}Ce_{1.8}O_7$ after 48 h TOS at (a, b) 700 °C, and (c, d) 800 °C.

The full recovery of all of the XANES features of the freshly calcined material occurs after re-oxidation at 700 °C, indicating a complete re-oxidation and dissolution of Ru (Figure 9a). In line with this, the FT and WT EXAFS data of the re-oxidized $Sm_2Ru_{0.2}Ce_{1.8}O_{7(800\text{-}DRM)}$ samples show only a peak due to the Ru–O shell but no signatures for a Ru–Ru shell, i.e., similar to the initial sloid solution (Figures 9b and S20a,b). The series of $Sm_2Ru_xCe_{2-x}O_{7(800\text{-}DRM)}$ (x = 0.1, 0.4) materials could also be re-oxidized in air (Figure S21). Again, only a peak due to the Ru-O shell was observed in the respective FT EXAFS spectra (Figure S21b,d). However, according to XANES spectra, the Ru loading influences the temperature when Ru is fully re-incorporation in the host oxide structure. For instance, $Sm_2Ru_{0.1}Ce_{1.9}O_7$ is re-oxidized at a lower temperature of 500 °C than $Sm_2Ru_{0.4}Ce_{1.6}O_7$ which is requiring 700 °C (Figures 9a and S21a,c). Comparison of the Raman spectra of $Sm_2Ru_{0.2}Ce_{1.8}O_7$ after re-oxidation at different temperatures with the calcined and reduced materials shows that the band at ca. 690 cm^{-1} (signature of the Ru dopant in the host lattice) vanishes after Ru exsolution and reappears after the re-incorporation of Ru above 500 °C (Figure 9c). Additionally, XRD results reveal that the superstructure-related peaks weaken and broaden with re-oxidation at temperatures ≥ 500 °C, due to the re-incorporation Ru (Figure 9d). Further discussion on re-oxidation tests using milder oxidizers such as CO_2 or a mixture of CO_2-steam (10 vol% H_2O) can be found in the supporting information (Figures S20 and S22). To conclude, experiments with $Sm_2Ru_{0.2}Ce_{1.8}O_{7(800\text{-}DRM)}$ confirm that dissolution of exsolved Ru can be utilized to effectively regenerate the catalyst by simple re-oxidation in air above 700 °C prior to a new exsolution cycle. Such repeated reduction and re-oxidation cycles can be performed at least twice without compromising the host structure (Figure S23).

4. CONCLUSIONS

Ru-based catalysts with a high activity for the dry reforming of methane and an enhanced thermal stability were prepared by the reductive exsolution of Ru(0) nanoparticles from the defective fluorite-type solid solution phases $Sm_2Ru_xCe_{2-x}O_7$ (x = 0.1, 0.2, or 0.4). The exsolution of very small Ru NPs with a size of approximately 1-2 nm transforms the defective fluorite $Sm_2Ru_{0.2}Ce_{1.8}O_7$ phase into a C-type structure Ru(0)/$Sm_2Ce_{1.8}O_{7-\delta}$ via a rearrangement of the oxygen vacancies that concentrate around the Ru atoms within the crystal lattice of $Sm_2Ru_{0.2}Ce_{1.8}O_7$. This transformation process is reversible, whereby the original structure can be restored by the dissolution of the exsolved Ru NPs via air oxidation at ≥ 700°C. Such Ru exsolution and dissolution cycles can be performed for at least two cycles. Overall, the reductive in situ exsolution is an efficient approach to yield catalysts with favourable features including high metal dispersion, very small particle size, and improved metal-support interaction ensuring an enhanced thermal stability of the material. Catalytic tests confirmed the superior performance of the catalysts prepared through the reductive exsolution approach, as compared to benchmark catalysts synthesized via wetness impregnation or sodium borohydride reduction methods.

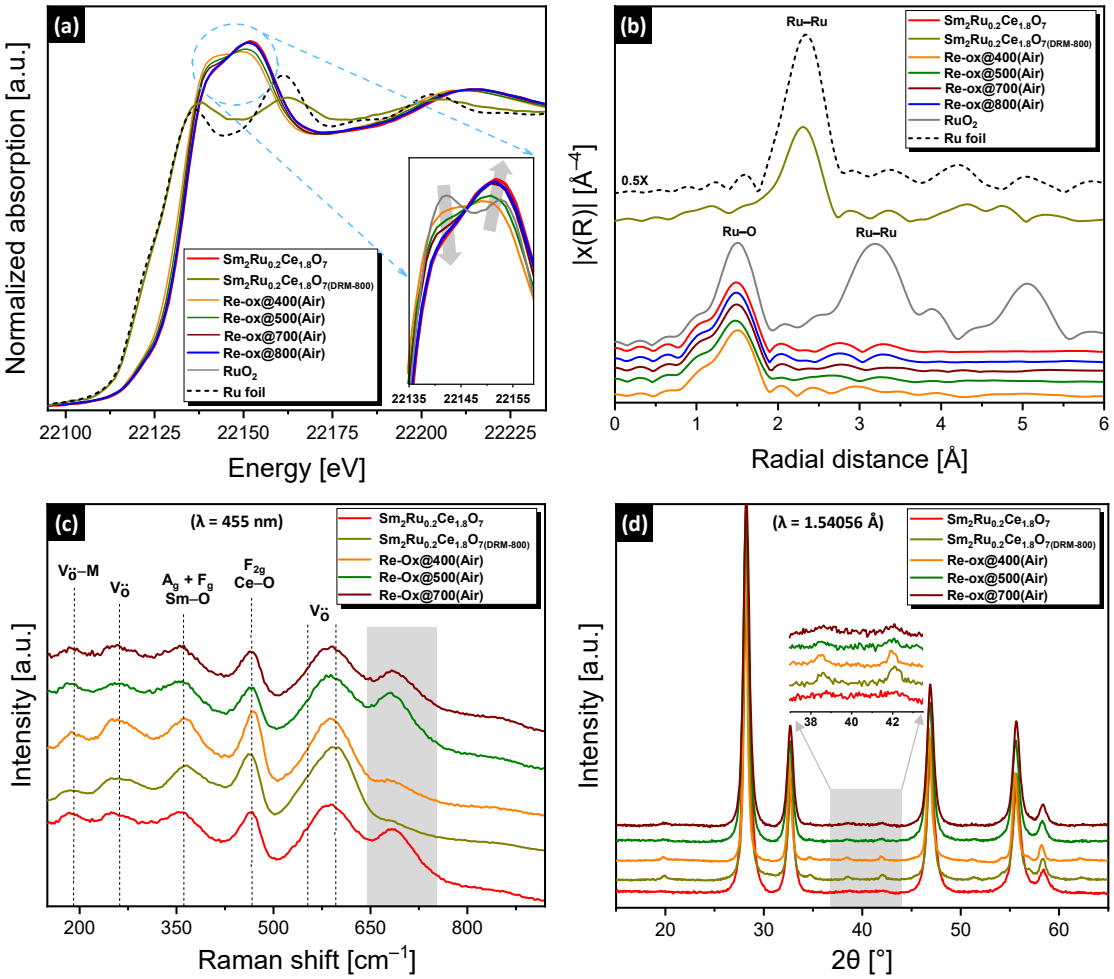

Figure 9. Ex situ Ru K-edge (a) XANES spectra, (b) FT of the k^3-weighted EXAFS data, (c) Raman spectra, and (d) XRD patterns (λ=0.49328 Å) of $Sm_2Ru_{0.2}Ce_{1.8}O_{7(DRM-800)}$ after re-oxidation in air at different temperatures. $Sm_2Ru_{0.2}Ce_{1.8}O_{7(DRM-800)}$ was pre-treated at 800 °C for 1 h in a DRM reaction mixture for each experiment. Re-oxidation was performed in the air (20 vol% O_2 in N_2).

ASSOCIATED CONTENT

Supporting Information

XRD, Raman, XAS and H_2-TPD data, Rietveld refinement and EXAFS fitting results, STEM-EDX images, catalytic activity results.

AUTHOR INFORMATION

Corresponding Author

*E-mail: abdalap@ethz.ch (P.M.A.).
*E-mail: muelchri@ethz.ch (C.R.M.).

Author Contributions

The manuscript was written through contributions of all authors. All authors have given approval to the final version of the manuscript.

Notes

The authors declare no competing financial interest.

ACKNOWLEDGMENT

The authors acknowledge the Scientific Center for Optical and Electron Microscopy (ScopeM) at ETH Zürich for the use of their electron microscopy facilities. ESRF and the Swiss Norwegian Beamlines (SNBL at ESRF) are gratefully acknowledged for providing access to the synchrotron facility. The authors would also like to thank Drs. Davood Hosseini, Qasim Imtiaz, and Xing Huang from ETH Zürich for performing TEM analysis and for fruitful discussions. Iurii Dovgaliuk is acknowledged for providing the high resolution XRD measurements at BM01, SNBL. Financial support from the Competence Center of Energy and Mobility (CCEM), ETH Zürich Career Seed Grant (SEED-02 17-2), Swiss National Science Foundation R'Equip grant (206021_144986), Swiss Grid, Stiftung Claude & Giuliana and the Swiss National Science Foundation (200020_156015) is greatly appreciated.

REFERENCES

1. Artz, J.; Müller, T. E.; Thenert, K.; Kleinekorte, J.; Meys, R.; Sternberg, A.; Bardow, A.; Leitner, W., Sustainable Conversion of Carbon Dioxide: An Integrated Review of Catalysis and Life Cycle Assessment. *Chem. Rev.* **2018,** *118*, 434-504.
2. Álvarez, A.; Bansode, A.; Urakawa, A.; Bavykina, A. V.; Wezendonk, T. A.; Makkee, M.; Gascon, J.; Kapteijn, F., Challenges in the Greener Production of Formates/Formic Acid, Methanol, and

DME by Heterogeneously Catalyzed CO_2 Hydrogenation Processes. *Chem. Rev.* **2017,** *117*, 9804-9838.
3. Wang, Y.; Yao, L.; Wang, S.; Mao, D.; Hu, C., Low-Temperature Catalytic CO_2 Dry Reforming of Methane on Ni-Based Catalysts: A Review. *Fuel Process. Technol.* **2018,** *169*, 199-206.
4. Abdulrasheed, A.; Jalil, A. A.; Gambo, Y.; Ibrahim, M.; Hambali, H. U.; Shahul Hamid, M. Y., A Review on Catalyst Development for Dry Reforming of Methane to Syngas: Recent Advances. *Renew. Sustain. Energy Rev.* **2019,** *108*, 175-193.
5. Buelens, L. C.; Galvita, V. V.; Poelman, H.; Detavernier, C.; Marin, G. B., Super-Dry Reforming of Methane Intensifies CO_2 Utilization Via Le Chatelier's Principle. *Science* **2016,** *354*, 449.
6. Ao, M.; Pham, G. H.; Sunarso, J.; Tade, M. O.; Liu, S., Active Centers of Catalysts for Higher Alcohol Synthesis from Syngas: A Review. *ACS Catal.* **2018,** *8*, 7025-7050.
7. Li, D.; Nakagawa, Y.; Tomishige, K., Methane Reforming to Synthesis Gas over Ni Catalysts Modified with Noble Metals. *Appl. Catal., A* **2011,** *408*, 1-24.
8. Fan, M.-S.; Abdullah, A. Z.; Bhatia, S., Catalytic Technology for Carbon Dioxide Reforming of Methane to Synthesis Gas. *ChemCatChem* **2009,** *1*, 192-208.
9. Theofanidis, S. A.; Galvita, V. V.; Poelman, H.; Marin, G. B., Enhanced Carbon-Resistant Dry Reforming Fe-Ni Catalyst: Role of Fe. *ACS Catal.* **2015,** *5*, 3028-3039.
10. Xie, T.; Shi, L.; Zhang, J.; Zhang, D., Immobilizing Ni Nanoparticles to Mesoporous Silica with Size and Location Control Via a Polyol-Assisted Route for Coking- and Sintering-Resistant Dry Reforming of Methane. *Chem. Commun.* **2014,** *50*, 7250-7253.
11. Zhang, X.; Zhang, L.; Peng, H.; You, X.; Peng, C.; Xu, X.; Liu, W.; Fang, X.; Wang, Z.; Zhang, N.; Wang, X., Nickel Nanoparticles Embedded in Mesopores of AlSBA-15 with a Perfect Peasecod-Like Structure: A Catalyst with Superior Sintering Resistance and Hydrothermal Stability for Methane Dry Reforming. *Appl. Catal., B* **2018,** *224*, 488-499.
12. Trimm, D. L., Catalysts for the Control of Coking During Steam Reforming. *Catal. Today* **1999,** *49*, 3-10.
13. Wang, S.; Lu, G. Q., Reforming of Methane with Carbon Dioxide over Ni/Al_2O_3 Catalysts: Effect of Nickel Precursor. *Appl. Catal., A* **1998,** *169*, 271-280.
14. Tomishige, K.; Himeno, Y.; Matsuo, Y.; Yoshinaga, Y.; Fujimoto, K., Catalytic Performance and Carbon Deposition Behavior of a NiO−MgO Solid Solution in Methane Reforming with Carbon Dioxide under Pressurized Conditions. *Ind. Eng. Chem. Res.* **2000,** *39*, 1891-1897.
15. Takanabe, K.; Nagaoka, K.; Nariai, K.; Aika, K.-i., Titania-Supported Cobalt and Nickel Bimetallic Catalysts for Carbon Dioxide Reforming of Methane. *J. Catal.* **2005,** *232*, 268-275.
16. Nair, M. M.; Kaliaguine, S.; Kleitz, F., Nanocast $LaNiO_3$ Perovskites as Precursors for the Preparation of Coke-Resistant Dry Reforming Catalysts. *ACS Catal.* **2014,** *4*, 3837-3846.
17. Lu, J.; Zhu, C.; Pan, C.; Lin, W.; Lemmon, J. P.; Chen, F.; Li, C.; Xie, K., Highly Efficient Electrochemical Reforming of CH_4/CO_2 in a Solid Oxide Electrolyser. *Sci. Adv.* **2018,** *4*.
18. Pakhare, D.; Spivey, J., A Review of Dry (CO_2) Reforming of Methane over Noble Metal Catalysts. *Chem. Soc. Rev.* **2014,** *43*, 7813-7837.
19. Margossian, T.; Larmier, K.; Kim, S. M.; Krumeich, F.; Fedorov, A.; Chen, P.; Müller, C. R.; Copéret, C., Molecularly Tailored Nickel Precursor and Support Yield a Stable Methane Dry Reforming Catalyst with Superior Metal Utilization. *J. Am. Chem. Soc.* **2017,** *139*, 6919-6927.
20. Kim, S. M.; Abdala, P. M.; Margossian, T.; Hosseini, D.; Foppa, L.; Armutlulu, A.; van Beek, W.; Comas-Vives, A.; Copéret, C.; Müller, C., Cooperativity and Dynamics Increase the Performance of NiFe Dry Reforming Catalysts. *J. Am. Chem. Soc.* **2017,** *139*, 1937-1949.
21. Kawi, S.; Kathiraser, Y.; Ni, J.; Oemar, U.; Li, Z.; Saw Eng, T., Progress in Synthesis of Highly Active and Stable Nickel-Based Catalysts for Carbon Dioxide Reforming of Methane. *ChemSusChem* **2015,** *8*, 3556-3575.
22. Tsoukalou, A.; Imtiaz, Q.; Kim, S. M.; Abdala, P. M.; Yoon, S.; Müller, C. R., Dry-Reforming of Methane over Bimetallic Ni–M/La_2O_3 (M=Co, Fe): The Effect of the Rate of $La_2O_2CO_3$ Formation and Phase Stability on the Catalytic Activity and Stability. *J. Catal.* **2016,** *343*, 208-214.
23. Rostrupnielsen, J. R.; Hansen, J. H. B., CO_2-Reforming of Methane over Transition Metals. *J. Catal.* **1993,** *144*, 38-49.
24. Wu, J.; Qiao, L.-Y.; Zhou, Z.-F.; Cui, G.-J.; Zong, S.-S.; Xu, D.-J.; Ye, R.-P.; Chen, R.-P.; Si, R.; Yao, Y.-G., Revealing the Synergistic Effects of Rh and Substituted $La_2B_2O_7$ (B = Zr or Ti) for Preserving the Reactivity of Catalyst in Dry Reforming of Methane. *ACS Catal.* **2019,** *9*, 932-945.
25. Hosseini, D.; Abdala, P. M.; Donat, F.; Kim, S. M.; Müller, C. R., Bifunctional Core-Shell Architecture Allows Stable H_2 Production Utilizing CH_4 and CO_2 in a Catalytic Chemical Looping Process. *Appl. Catal., B* **2019,** *258*, 117946.
26. Li, Y.; Jiang, J.; Zhu, C.; Li, L.; Li, Q.; Ding, Y.; Yang, W., The Enhanced Catalytic Performance and Stability of $Rh/\gamma\text{-}Al_2O_3$ Catalyst Synthesized by Atomic Layer Deposition (ALD) for Methane Dry Reforming. *Materials* **2018,** *11*, 172.
27. Liu, Z.; Zhang, F.; Rui, N.; Li, X.; Lin, L.; Betancourt, L. E.; Su, D.; Xu, W.; Cen, J.; Attenkofer, K.; Idriss, H.; Rodriguez, J. A.; Senanayake, S. D., Highly Active Ceria-Supported Ru Catalyst for the Dry Reforming of Methane: In Situ Identification of $Ru^{\delta+}$–Ce^{3+} Interactions for Enhanced Conversion. *ACS Catal.* **2019,** *9*, 3349-3359.
28. da Fonseca, R. O.; Garrido, G. S.; Rabelo-Neto, R. C.; Silveira, E. B.; Simões, R. C. C.; Mattos, L. V.; Noronha, F. B., Study of the Effect of Gd-Doping Ceria on the Performance of $Pt/GdCeO_2/Al_2O_3$ Catalysts for the Dry Reforming of Methane. *Catal. Today* **2019**. (doi.org/10.1016/j.cattod.2019.04.079)
29. Singh, S.; Zubenko, D.; Rosen, B. A., Influence of $LaNiO_3$ Shape on Its Solid-Phase Crystallization into Coke-Free Reforming Catalysts. *ACS Catal.* **2016,** *6*, 4199-4205.
30. Tauster, S. J., Strong Metal-Support Interactions. *Acc. Chem. Res.* **1987,** *20*, 389-394.
31. De Rogatis, L.; Cargnello, M.; Gombac, V.; Lorenzut, B.; Montini, T.; Fornasiero, P., Embedded Phases: A Way to Active and Stable Catalysts. *ChemSusChem* **2009,** *3*, 24-42.
32. Liang, X.; Li, J.; Yu, M.; McMurray, C. N.; Falconer, J. L.; Weimer, A. W., Stabilization of Supported Metal Nanoparticles Using an Ultrathin Porous Shell. *ACS Catal.* **2011,** *1*, 1162-1165.
33. Kim, D. H.; Kim, S. Y.; Han, S. W.; Cho, Y. K.; Jeong, M.-G.; Park, E. J.; Kim, Y. D., The Catalytic Stability of TiO_2-Shell/Ni-Core Catalysts for CO_2 Reforming of CH_4. *Appl. Catal., A* **2015,** *495*, 184-191.
34. Cheng, N.; Banis Mohammad, N.; Liu, J.; Riese, A.; Li, X.; Li, R.; Ye, S.; Knights, S.; Sun, X., Extremely Stable Platinum Nanoparticles Encapsulated in a Zirconia Nanocage by Area-Selective Atomic Layer Deposition for the Oxygen Reduction Reaction. *Adv. Mater.* **2014,** *27*, 277-281.
35. Liu, X.; Zhu, Q.; Lang, Y.; Cao, K.; Chu, S.; Shan, B.; Chen, R., Oxide-Nanotrap-Anchored Platinum Nanoparticles with High Activity and Sintering Resistance by Area-Selective Atomic Layer Deposition. *Angew. Chem. Int. Ed.* **2017,** *129*, 1670-1674.
36. Neagu, D.; Oh, T.-S.; Miller, D. N.; Ménard, H.; Bukhari, S. M.; Gamble, S. R.; Gorte, R. J.; Vohs, J. M.; Irvine, J. T. S., Nano-Socketed Nickel Particles with Enhanced Coking Resistance Grown in Situ by Redox Exsolution. *Nat. Commun.* **2015,** *6*, 8120.
37. Nishihata, Y.; Mizuki, J.; Akao, T.; Tanaka, H.; Uenishi, M.; Kimura, M.; Okamoto, T.; Hamada, N., Self-Regeneration of a Pd-Perovskite Catalyst for Automotive Emissions Control. *Nature* **2002,** *418*, 164.
38. Neagu, D.; Tsekouras, G.; Miller, D. N.; Ménard, H.; Irvine, J. T. S., In Situ Growth of Nanoparticles through Control of Non-Stoichiometry. *Nat. Chem.* **2013,** *5*, 916.
39. Wei, H.; Xie, K.; Zhang, J.; Zhang, Y.; Wang, Y.; Qin, Y.; Cui, J.; Yan, J.; Wu, Y., In Situ Growth of Ni_xCu_{1-x} Alloy Nanocatalysts on Redox-Reversible Rutile $(Nb,Ti)O_4$ Towards High-Temperature Carbon Dioxide Electrolysis. *Sci. Rep.* **2014,** *4*, 5156.
40. Steiger, P.; Delmelle, R.; Foppiano, D.; Holzer, L.; Heel, A.; Nachtegaal, M.; Kröcher, O.; Ferri, D., Structural Reversibility and Nickel Particle Stability in Lanthanum Iron Nickel Perovskite-Type Catalysts. *ChemSusChem* **2017,** *10*, 2505-2517.
41. Kwon, O.; Sengodan, S.; Kim, K.; Kim, G.; Jeong, H. Y.; Shin, J.; Ju, Y.-W.; Han, J. W.; Kim, G., Exsolution Trends and Co-

Segregation Aspects of Self-Grown Catalyst Nanoparticles in Perovskites. *Nat. Commun.* **2017,** *8*, 15967.
42. Steiger, P.; Nachtegaal, M.; Kröcher, O.; Ferri, D., Reversible Segregation of Ni in $LaFe_{0.8}Ni_{0.2}O_{3\pm\delta}$ During Coke Removal. *ChemCatChem* **2018,** *10*, 4456-4464.
43. Millet, M.-M.; Tarasov, A. V.; Girgsdies, F.; Algara-Siller, G.; Schlögl, R.; Frei, E., Highly Dispersed $Ni^0/Ni_xMg_{1-x}O$ Catalysts Derived from Solid Solutions: How Metal and Support Control the CO_2 Hydrogenation. *ACS Catal.* **2019**, 8534-8546.
44. Joo, S.; Kwon, O.; Kim, K.; Kim, S.; Kim, H.; Shin, J.; Jeong, H. Y.; Sengodan, S.; Han, J. W.; Kim, G., Cation-Swapped Homogeneous Nanoparticles in Perovskite Oxides for High power Density. *Nat. Commun.* **2019,** *10*, 697.
45. Steiger, P.; Burnat, D.; Madi, H.; Mai, A.; Holzer, L.; Van Herle, J.; Kröcher, O.; Heel, A.; Ferri, D., Sulfur Poisoning Recovery on a Solid Oxide Fuel Cell Anode Material through Reversible Segregation of Nickel. *Chem. Mater.* **2019,** *31*, 748-758.
46. Gao, Y.; Lu, Z.; You, T. L.; Wang, J.; Xie, L.; He, J.; Ciucci, F., Energetics of Nanoparticle Exsolution from Perovskite Oxides. *J. Phys. Chem. Lett.* **2018,** *9*, 3772-3778.
47. Ye, L.; Zhang, M.; Huang, P.; Guo, G.; Hong, M.; Li, C.; Irvine, J. T. S.; Xie, K., Enhancing CO_2 Electrolysis through Synergistic Control of Non-Stoichiometry and Doping to Tune Cathode Surface Structures. *Nat. Commun.* **2017,** *8*, 14785.
48. Neagu, D.; Papaioannou, E. I.; Ramli, W. K. W.; Miller, D. N.; Murdoch, B. J.; Ménard, H.; Umar, A.; Barlow, A. J.; Cumpson, P. J.; Irvine, J. T. S.; Metcalfe, I. S., Demonstration of Chemistry at a Point through Restructuring and Catalytic Activation at Anchored Nanoparticles. *Nat. Commun.* **2017,** *8*, 1855.
49. Katz, M. B.; Graham, G. W.; Duan, Y.; Liu, H.; Adamo, C.; Schlom, D. G.; Pan, X., Self-Regeneration of Pd–$LaFeO_3$ Catalysts: New Insight from Atomic-Resolution Electron Microscopy. *J. Am. Chem. Soc.* **2011,** *133*, 18090-18093.
50. Katz, M. B.; Zhang, S.; Duan, Y.; Wang, H.; Fang, M.; Zhang, K.; Li, B.; Graham, G. W.; Pan, X., Reversible Precipitation/Dissolution of Precious-Metal Clusters in Perovskite-Based Catalyst Materials: Bulk Versus Surface Re-Dispersion. *J. Catal.* **2012,** *293*, 145-148.
51. Kalland, L.-E.; Norberg, S. T.; Kyrklund, J.; Hull, S.; Eriksson, S. G.; Norby, T.; Mohn, C. E.; Knee, C. S., C-Type Related Order in the Defective Fluorites $La_2Ce_2O_7$ and $Nd_2Ce_2O_7$ Studied by Neutron Scattering and Ab Initio MD Simulations. *Phys. Chem. Chem. Phys.* **2016,** *18*, 24070-24080.
52. Polo-Garzon, F.; Scott, J. K.; Bruce, D. A., Microkinetic Model for the Dry Reforming of Methane on Rh Doped Pyrochlore Catalysts. *J. Catal.* **2016,** *340*, 196-204.
53. le Saché, E.; Pastor-Pérez, L.; Watson, D.; Sepúlveda-Escribano, A.; Reina, T. R., Ni Stabilised on Inorganic Complex Structures: Superior Catalysts for Chemical CO_2 Recycling Via Dry Reforming of Methane. *Appl. Catal., B* **2018,** *236*, 458-465.
54. Tian, J.; Peng, H.; Xu, X.; Liu, W.; Ma, Y.; Wang, X.; Yang, X., High Surface Area $La_2Sn_2O_7$ Pyrochlore as a Novel, Active and Stable Support for Pd for CO Oxidation. *Catal. Sci. Technol.* **2015,** *5*, 2270-2281.
55. Oemar, U.; Hidajat, K.; Kawi, S., Pd–Ni Catalyst over Spherical Nanostructured Y_2O_3 Support for Oxy-CO_2 Reforming of Methane: Role of Surface Oxygen Mobility. *Int. J. Hydrogen Energy* **2015,** *40*, 12227-12238.
56. Xu, J.; Peng, L.; Fang, X.; Fu, Z.; Liu, W.; Xu, X.; Peng, H.; Zheng, R.; Wang, X., Developing Reactive Catalysts for Low Temperature Oxidative Coupling of Methane: On the Factors Deciding the Reaction Performance of $Ln_2Ce_2O_7$ with Different Rare Earth a Sites. *Appl. Catal., A* **2018,** *552*, 117-128.
57. Montini, T.; Melchionna, M.; Monai, M.; Fornasiero, P., Fundamentals and Catalytic Applications of CeO_2-Based Materials. *Chem. Rev.* **2016,** *116*, 5987-6041.
58. Małecka, M. A., Ceria-Based Mixed Oxides–Beautiful Structures. *ChemistrySelect* **2016,** *1*, 4246-4254.
59. Zhang, Q.; Zheng, X.; Jiang, J.; Liu, W., Structural Stability of $La_2Ce_2O_7$ as a Proton Conductor: A First-Principles Study. *J. Phys. Chem. C* **2013,** *117*, 20379-20386.
60. Coduri, M.; Checchia, S.; Longhi, M.; Ceresoli, D.; Scavini, M., Rare Earth Doped Ceria: The Complex Connection between Structure and Properties. *Front. Chem.* **2018,** *6*, 526.
61. Momma, K.; Izumi, F., Vesta: A Three-Dimensional Visualization System for Electronic and Structural Analysis. *J. Appl. Crystallogr.* **2008,** *41*, 653-658.
62. Hsieh, H.-C.; Chang, Y.-C.; Tsai, P.-W.; Lin, Y.-Y.; Chuang, Y.-C.; Sheu, H.-S.; Lee, C.-S., Metal Substituted Pyrochlore Phase $Li_xLa_{2-x}Ce_{1.8}Ru_{0.2}O_{7-\delta}$ (X = 0.0–0.6) as an Effective Catalyst for Oxidative and Auto-Thermal Steam Reforming of Ethanol. *Catal. Sci. Technol.* **2019,** *9*, 1406-1419.
63. McFarland, E. W.; Metiu, H., Catalysis by Doped Oxides. *Chem. Rev.* **2013,** *113*, 4391-4427.
64. Dyadkin, V.; Pattison, P.; Dmitriev, V.; Chernyshov, D., A New Multipurpose Diffractometer Pilatus@Snbl. *J. Synchrotron Rad.* **2016,** *23*, 825-829.
65. Rodríguez-Carvajal, J., Recent Advances in Magnetic Structure Determination by Neutron Powder Diffraction. *Physica B: Condensed Matter* **1993,** *192*, 55-69.
66. van Beek, W.; Safonova, O. V.; Wiker, G.; Emerich, H., Snbl, a Dedicated Beamline for Combined in Situ X-Ray Diffraction, X-Ray Absorption and Raman Scattering Experiments. *Phase Transitions* **2011,** *84*, 726-732.
67. Abdala, P. M.; Mauroy, H.; van Beek, W., A Large-Area CMOS Detector for High-Energy Synchrotron Powder Diffraction and Total Scattering Experiments. *J. Appl. Crystallogr.* **2014,** *47*, 449-457.
68. Kieffer, J.; Wright, J. P., Pyfai: A Python Library for High Performance Azimuthal Integration on GPU. *Powder Diffr.* **2013,** *28*, S339-S350.
69. Ravel, B.; Newville, M., Athena, Artemis, Hephaestus: Data Analysis for X-Ray Absorption Spectroscopy Using IFEFFIT. *J. Synchrotron Radiat.* **2005,** *12*, 537-541.
70. Sakpal, T.; Lefferts, L., Structure-Dependent Activity of CeO_2 Supported Ru Catalysts for CO_2 Methanation. *J. Catal.* **2018,** *367*, 171-180.
71. Goodwin, J. G., Characterization of Highly Dispersed Ru Catalysts by Chemisorption. *J. Catal.* **1981,** *68*, 227-232.
72. Yamamura, H.; Nishino, H.; Kakinuma, K.; Nomura, K., Crystal Phase and Electrical Conductivity in the Pyrochlore-Type Composition Systems, $Ln_2Ce_2O_7$ (Ln=La, Nd, Sm, Eu, Gd, Y and Yb). *J. Ceram. Soc. Jpn.* **2003,** *111*, 902-906.
73. Coduri, M.; Masala, P.; Allieta, M.; Peral, I.; Brunelli, M.; Biffi, C. A.; Scavini, M., Phase Transformations in the CeO_2–Sm_2O_3 System: A Multiscale Powder Diffraction Investigation. *Inorg. Chem.* **2018,** *57*, 879-891.
74. Chen, S.-Y.; Chen, R.-J.; Lee, W.; Dong, C.-L.; Gloter, A., Spectromicroscopic Evidence of Interstitial and Substitutional Dopants in Association with Oxygen Vacancies in Sm-Doped Ceria Nanoparticles. *Phys. Chem. Chem. Phys.* **2014,** *16*, 3274-3281.
75. Murgida, G. E.; Ferrari, V.; Ganduglia-Pirovano, M. V.; Llois, A. M., Ordering of Oxygen Vacancies and Excess Charge Localization in Bulk Ceria: A DFT+U Study. *Phys. Rev. B* **2014,** *90*, 115120.
76. Dvořák, F.; Szabová, L.; Johánek, V.; Farnesi Camellone, M.; Stetsovych, V.; Vorokhta, M.; Tovt, A.; Skála, T.; Matolínová, I.; Tateyama, Y.; Mysliveček, J.; Fabris, S.; Matolín, V., Bulk Hydroxylation and Effective Water Splitting by Highly Reduced Cerium Oxide: The Role of O Vacancy Coordination. *ACS Catal.* **2018,** *8*, 4354-4363.
77. Coduri, M.; Scavini, M.; Allieta, M.; Brunelli, M.; Ferrero, C., Defect Structure of Y-Doped Ceria on Different Length Scales. *Chem. Mater.* **2013,** *25*, 4278-4289.
78. Singh, P.; Hegde, M. S., $Ce_{1-x}Ru_xO_{2-\delta}$ (X=0.05, 0.10): A New High Oxygen Storage Material and Pt, Pd-Free Three-Way Catalyst. *Chem. Mater.* **2009,** *21*, 3337-3345.
79. Sharma, S.; Hu, Z.; Zhang, P.; McFarland, E. W.; Metiu, H., CO_2 Methanation on Ru-Doped Ceria. *J. Catal.* **2011,** *278*, 297-309.
80. Horlait, D.; Claparède, L.; Clavier, N.; Szenknect, S.; Dacheux, N.; Ravaux, J.; Podor, R., Stability and Structural Evolution of $Ce^{iv}_{1-x}Ln^{iii}_xO_{2-x/2}$ Solid Solutions: A Coupled μ-Raman/XRD Approach. *Inorg. Chem.* **2011,** *50*, 7150-7161.
81. Yamamura, H.; Nishino, H.; Kakinuma, K.; Nomura, K., Relationship between Oxide-Ion Conductivity and Ordering of Oxide Ion in the $(Y_{1-x}La_x)_2(Ce_{1-x}Zr_x)_2O_7$ System with Pyrochlore-Type Composition. *Solid State Ion.* **2007,** *178*, 233-238.
82. Artini, C.; Pani, M.; Carnasciali, M. M.; Buscaglia, M. T.; Plaisier, J. R.; Costa, G. A., Structural Features of Sm- and Gd-Doped Ceria

Studied by Synchrotron X-Ray Diffraction and μ-Raman Spectroscopy. *Inorg. Chem.* **2015,** *54*, 4126-4137.
83. Jampaiah, D.; Tur, K. M.; Ippolito, S. J.; Sabri, Y. M.; Tardio, J.; Bhargava, S. K.; Reddy, B. M., Structural Characterization and Catalytic Evaluation of Transition and Rare Earth Metal Doped Ceria-Based Solid Solutions for Elemental Mercury Oxidation. *RSC Adv.* **2013,** *3*, 12963-12974.
84. Huang, H.; Dai, Q.; Wang, X., Morphology Effect of Ru/CeO_2 Catalysts for the Catalytic Combustion of Chlorobenzene. *Appl. Catal., B* **2014,** *158-159*, 96-105.
85. Lee, J.; Ryou, Y.; Chan, X.; Kim, T. J.; Kim, D. H., How Pt Interacts with CeO_2 under the Reducing and Oxidizing Environments at Elevated Temperature: The Origin of Improved Thermal Stability of Pt/CeO_2 Compared to CeO_2. *J. Phys. Chem. C* **2016,** *120*, 25870-25879.
86. Gu, Y.; Jiang, X.; Sun, W.; Bai, S.; Dai, Q.; Wang, X., 1,2-Dichloroethane Deep Oxidation over Bifunctional Ru/Ce_xAl_y Catalysts. *ACS Omega* **2018,** *3*, 8460-8470.
87. Mar, S. Y.; Chen, C. S.; Huang, Y. S.; Tiong, K. K., Characterization of RuO_2 Thin Films by Raman Spectroscopy. *Appl. Surf. Sci.* **1995,** *90*, 497-504.
88. Searles, K.; Siddiqi, G.; Safonova, O. V.; Copéret, C., Silica-Supported Isolated Gallium Sites as Highly Active, Selective and Stable Propane Dehydrogenation Catalysts. *Chem. Sci* **2017,** *8*, 2661-2666.
89. Lebedev, D.; Povia, M.; Waltar, K.; Abdala, P. M.; Castelli, I. E.; Fabbri, E.; Blanco, M. V.; Fedorov, A.; Copéret, C.; Marzari, N.; Schmidt, T. J., Highly Active and Stable Iridium Pyrochlores for Oxygen Evolution Reaction. *Chem. Mater.* **2017,** *29*, 5182-5191.
90. Baidya, T.; Bera, P.; Kröcher, O.; Safonova, O.; Abdala, P. M.; Gerke, B.; Pöttgen, R.; Priolkar, K. R.; Mandal, T. K., Understanding the Anomalous Behavior of Vegard's Law in $Ce_{1-x}M_xO_2$ (M = Sn and Ti; $0 < X \leq 0.5$) Solid Solutions. *Phys. Chem. Chem. Phys.* **2016,** *18*, 13974-13983.
91. Eyssler, A.; Mandaliev, P.; Winkler, A.; Hug, P.; Safonova, O.; Figi, R.; Weidenkaff, A.; Ferri, D., The Effect of the State of Pd on Methane Combustion in Pd-Doped $LaFeO_3$. *J. Phys. Chem. C* **2010,** *114*, 4584-4594.
92. Wu, T. S.; Li, H. D.; Chen, Y. W.; Chen, S. F.; Su, Y. S.; Chu, C. H.; Pao, C. W.; Lee, J. F.; Lai, C. H.; Jeng, H. T.; Chang, S. L.; Soo, Y. L., Unconventional Interplay between Heterovalent Dopant Elements: Switch-and-Modulator Band-Gap Engineering in (Y, Co)-Codoped CeO_2 Nanocrystals. *Sci. Rep.* **2015,** *5*, 15415.
93. Chen, H.-T., First-Principles Study of CO Adsorption and Oxidation on Ru-Doped CeO_2(111) Surface. *J. Phys. Chem. C* **2012,** *116*, 6239-6246.
94. Ohashi, T.; Yamazaki, S.; Tokunaga, T.; Arita, Y.; Matsui, T.; Harami, T.; Kobayashi, K., Exafs Study of $Ce_{1-x}Gd_xO_{2-x/2}$. *Solid State Ion.* **1998,** *113-115*, 559-564.
95. Yamazaki, S.; Matsui, T.; Ohashi, T.; Arita, Y., Defect Structures in Doped CeO_2 Studied by Using XAFS Spectrometry. *Solid State Ion.* **2000,** *136-137*, 913-920.
96. Giannici, F.; Gregori, G.; Aliotta, C.; Longo, A.; Maier, J.; Martorana, A., Structure and Oxide Ion Conductivity: Local Order, Defect Interactions and Grain Boundary Effects in Acceptor-Doped Ceria. *Chem. Mater.* **2014,** *26*, 5994-6006.
97. Kraynis, O.; Timoshenko, J.; Huang, J.; Singh, H.; Wachtel, E.; Frenkel, A. I.; Lubomirsky, I., Modeling Strain Distribution at the Atomic Level in Doped Ceria Films with Extended X-Ray Absorption Fine Structure Spectroscopy. *Inorg. Chem.* **2019,** *58*, 7527-7536.
98. Karim, A. M.; Prasad, V.; Mpourmpakis, G.; Lonergan, W. W.; Frenkel, A. I.; Chen, J. G.; Vlachos, D. G., Correlating Particle Size and Shape of Supported Ru/γ-Al_2O_3 Catalysts with NH_3 Decomposition Activity. *J. Am. Chem. Soc.* **2009,** *131*, 12230-12239.
99. Quek, X.-Y.; Filot, I. A. W.; Pestman, R.; van Santen, R. A.; Petkov, V.; Hensen, E. J. M., Correlating Fischer–Tropsch Activity to Ru Nanoparticle Surface Structure as Probed by High-Energy X-Ray Diffraction. *Chem. Commun.* **2014,** *50*, 6005-6008.
100. Zhang, Z.; Wu, Q.; Johnson, G.; Ye, Y.; Li, X.; Li, N.; Cui, M.; Lee, J. D.; Liu, C.; Zhao, S.; Li, S.; Orlov, A.; Murray, C. B.; Zhang, X.; Gunnoe, T. B.; Su, D.; Zhang, S., Generalized Synthetic Strategy for Transition-Metal-Doped Brookite-Phase TiO_2 Nanorods. *J. Am. Chem. Soc.* **2019,** *141*, 16548-16552.
101. Zhou, H.; Zhang, T.; Sui, Z.; Zhu, Y.-A.; Han, C.; Zhu, K.; Zhou, X., A Single Source Method to Generate Ru-Ni-MgO Catalysts for Methane Dry Reforming and the Kinetic Effect of Ru on Carbon Deposition and Gasification. *Appl. Catal., B* **2018,** *233*, 143-159.

Graphical Abstract

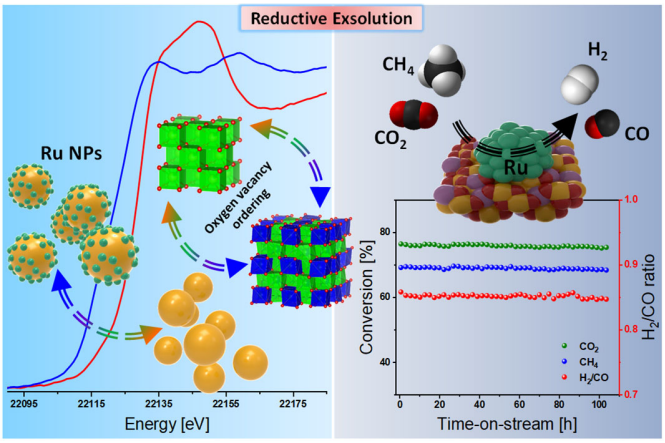

Nanoparticles from atoms in an oxide lattice: reductive exsolution of Ru from fluorite-type $Sm_2RuxCe_{2-x}O_7$ yields Ru(0) nanoparticles of 1-2 nm in diameter uniformly dispersed on the oxide support, accompanied by rearrangement of oxygen vacancies within the oxide lattice. Resulting material shows a remarkable stability for the dry reforming of methane.